

1 **Mechanistic investigations of the formation of highly oxidized**  
2 **products from the multi-generation OH oxidation of styrene**

3 Long Chen,<sup>1,2,3</sup> Yu Huang,<sup>\*,1,2,3</sup> Yonggang Xue,<sup>1,2,3</sup> Long Cui,<sup>1,2,3,5</sup> Zhihui Jia<sup>4</sup>

4 <sup>1</sup> *State Key Laboratory of Loess Science, Institute of Earth Environment, Chinese*  
5 *Academy of Sciences, Xi'an 710061, China*

6 <sup>2</sup> *National Observation and Research Station of Regional Ecological Environment*  
7 *Change and Comprehensive Management in the Guanzhong Plain, Xi'an 710061,*  
8 *China*

9 <sup>3</sup> *Shaanxi Key Laboratory of Atmospheric and Haze-fog Pollution Prevention, Xi'an*  
10 *710061, China*

11 <sup>4</sup> *School of Materials Science and Engineering, Shaanxi Normal University, Xi'an,*  
12 *Shaanxi, 710119, China*

13 <sup>5</sup> *School of Environmental Science and Engineering, Hubei Key Laboratory of Mine*  
14 *Environmental, Pollution Control and Remediation, Hubei Polytechnic University,*  
15 *Huangshi 435003, China*

16

17

18 Submitted to *Atmospheric Chemistry & Physics*

19

20

21 \*Corresponding author:

22 Prof. Yu Huang, E-mail address: [huangyu@ieecas.cn](mailto:huangyu@ieecas.cn)

23

## 24 Abstract

25 Styrene is the second most efficient aromatic compound in the formation of  
26 secondary organic aerosol (SOA) after toluene. Recent experiments have identified C<sub>7</sub>  
27 and C<sub>8</sub> series compounds as the main components of SOA in the photooxidation of  
28 styrene. However, their molecular structures and formation pathways remain largely  
29 uncharacterized. Herein, the formation mechanisms of highly oxidized products from  
30 the multi-generation OH oxidation of styrene are studied using the quantum  
31 chemistry methods. The calculations show that the addition of OH radicals to the  
32 C<sub>β</sub>-site of vinyl group is the dominant pathway, with benzaldehyde, 1<sup>st</sup>-ROOH  
33 (C<sub>8</sub>H<sub>10</sub>O<sub>3</sub>) and 1<sup>st</sup>-RONO<sub>2</sub> (C<sub>8</sub>H<sub>9</sub>NO<sub>3</sub>) being the main closed-shell C<sub>7</sub>- and  
34 C<sub>8</sub>-products in the first generation OH oxidation. For the second generation OH  
35 oxidation, OH-addition reaction occurring at the C<sub>1</sub>-site of 1<sup>st</sup>-ROOH and 1<sup>st</sup>-RONO<sub>2</sub>  
36 has a significant dominance. The resulting peroxide bicyclic peroxy radicals (BPR)  
37 can react with HO<sub>2</sub> radicals and NO to form the closed-shell C<sub>8</sub>-products 2<sup>nd</sup>-ROOH  
38 (C<sub>8</sub>H<sub>12</sub>O<sub>8</sub>) and 2<sup>nd</sup>-RONO<sub>2</sub> (C<sub>8</sub>H<sub>10</sub>N<sub>2</sub>O<sub>10</sub>), with the fractional yields of 41.4% and  
39 4.8%. The peroxide bicyclic alkoxy radical (BAR) can proceed either the  
40 ring-opening reactions to form the dicarbonyl C<sub>4</sub>-species, or undergo the cyclization  
41 reactions to generate the highly oxidized C<sub>6</sub>-epoxides. For the third generation OH  
42 oxidation, *syn*-OH-addition occurring at the C=C double bond of 2<sup>nd</sup>-ROOH and  
43 2<sup>nd</sup>-RONO<sub>2</sub> has the smallest barrier. The major closed-shell C<sub>8</sub>-products are the  
44 multifunctional hydroperoxides and organic nitrates which possess a peroxide bridge,  
45 two carbonyls, and two hydroxy. The volatility of the multi-generation OH oxidation  
46 products significantly decreases with increasing the number of OH oxidation steps.

47

## 48 1. Introduction

49 Aromatic compounds are recognized as the significant secondary organic aerosol  
50 (SOA) precursors, accounting for 20%-30% of the total volatile organic compounds  
51 (VOCs) and up to ~60% of the urban atmosphere (Xu et al., 2020; Yan et al., 2019; Yu  
52 et al., 2022; Cabrera-Perez et al., 2016; Iyer et al., 2023; Wang et al., 2017; Bloss et

53 al., 2005; Forstner et al., 1997). The primary sources include the incomplete  
54 combustion, solvent evaporation, and industrial emission, and the secondary sources  
55 involve the biofuel and biomass burning (Xu et al., 2020; Cabrera-Perez et al., 2016;  
56 Li et al., 2019). The most abundant aromatic compounds, including benzene, toluene,  
57 ethylbenzene, xylenes, styrene and trimethylbenzenes, are highly present in urban  
58 environments (Cabrera-Perez et al., 2016; Koppmann, 2008). The degradation of  
59 aromatic compounds initiated by the atmospheric oxidants (e.g., OH radicals, NO<sub>3</sub>  
60 radicals, O<sub>3</sub>, and Cl atom) leads to the formation of the highly oxidized products (e.g.,  
61 nitroaromatics, dicarbonyls, cresols, epoxides) (Ji et al., 2017; Wu et al., 2014; Fu et  
62 al., 2023; Wang and Li, 2021; Wang et al., 2013; Zaytsev et al., 2019; Wang et al.,  
63 2020), significantly contributing to new particle formation (NPF) and SOA formation  
64 (up to 50% in eastern China) in the atmosphere (Wang et al., 2017; Wang et al., 2020;  
65 Garmash et al., 2020; Molteni et al., 2018; Nie et al., 2022).

66 Styrene has been identified as the second most efficient aromatic compound in  
67 the formation of SOA after toluene (Sun et al., 2006; Tajuelo et al., 2019a), which is  
68 primarily emitted from the anthropogenic activities such as solvent usage and vehicle  
69 exhaust (Cho et al., 2014; Wu et al., 2021). Styrene is detected at the ppb levels in  
70 urban environments, with the mixing ratios of 0.06-4.50 ppb (Cho et al., 2014; Huang  
71 et al., 2019), which has been classified as a hazardous air pollutant in the 1990 Clean  
72 Air Act due to the potential mutagen and carcinogen (Environmental Protection  
73 Agency (EPA), 1990). Therefore, it is very necessary to investigate the degradation  
74 mechanisms of styrene under atmospheric conditions. In general, the atmospheric  
75 oxidation of styrene initiated by OH radicals is anticipated to be the dominant daytime  
76 sink, and the lifetime is estimated to be ~ 8 h under the conditions of typical OH  
77 radicals concentrations ( $[OH] = \sim 2 \times 10^6$  molecules cm<sup>-3</sup>) (Wu et al., 2021; Shen et  
78 al., 2022). Due to the existence of highly reactive vinyl and aromatic groups,  
79 OH-initiated oxidation of styrene mainly comprise two kinds of pathways:  
80 H-abstraction and OH-addition, in which C<sub>β</sub>-site OH-addition reaction is expected to  
81 be the predominant pathway (Wu et al., 2021; Wang et al., 2015; Zhang et al., 2024).  
82 The formed products can combine with an O<sub>2</sub> molecule leading to the first generation

83 peroxy radicals, which can further react with NO resulting in the formation of  
84 benzaldehyde and formaldehyde. The barrier of the rate-limiting step is predicted to  
85 be 28.4 kcal/mol (Wang et al., 2015), implying that benzaldehyde is unlikely to be the  
86 sole primary product in the oxidation of styrene due to their higher barriers.  
87 Additionally, carbonyl oxides, formed in the ozonolysis of styrene, serve as the chain  
88 units participating in the formation of oligomers (Yu et al., 2022). The volatility of  
89 oligomers decreases dramatically as the successive addition of carbonyl oxides  
90 increases, eventually transforming into extremely low volatility organic compounds  
91 (ELVOC) and directly participating in NPF.

92 Experimentally, Cho et al., investigated the kinetics of the reaction styrene  
93 + OH at 240-340 K and 1-3 Torr using the mass spectrometry technique (Cho et al.,  
94 2014). They found that the addition of OH radicals to the vinyl carbons is dominant,  
95 and the determined rate coefficient is  $(5.80 \pm 0.49) \times 10^{-11} \text{ cm}^3 \text{ molecule}^{-1} \text{ s}^{-1}$  at room  
96 temperature. In the smog chamber experiments, Tajuelo et al., (2019a, 2019b and  
97 2019c) found that the SOA yields from the photolysis and photooxidation of styrene  
98 and its homologous species increase with the concentration of initial reactants  
99 increasing, and benzaldehyde, benzoyl chloride, acetophenone and formaldehyde are  
100 expected to be the primary gas phase products. Yu et al. (2022) investigated the  
101 formation of SOA from styrene in an indoor chamber under different NO<sub>x</sub> and RH  
102 conditions, and found the SOA yields decrease with increasing RH in both the H<sub>2</sub>O<sub>2</sub>  
103 and NO<sub>x</sub> systems. The C<sub>7</sub> and C<sub>8</sub> species are the main products in the H<sub>2</sub>O<sub>2</sub> system,  
104 while organic nitrates are the major components in the NO<sub>x</sub> system. Although the  
105 possible molecular formula and chemical composition of the oxidation products from  
106 the reaction styrene + OH are given in the aforementioned studies, the specific  
107 molecular structures and formation pathways remain ambiguous. Additionally, to the  
108 best of our knowledge, the majority of studies mainly focus on the first  
109 generation OH oxidation products to date, while the formation mechanisms of highly  
110 oxidized products from the multi-generation OH oxidation of styrene are still limited.

111 In the present study, the multi-generation OH oxidation mechanisms of styrene  
112 in the presence of HO<sub>2</sub> /NO are investigated using the quantum chemistry methods.

113 The calculated results arising from the first generation OH oxidation reactions are  
114 presented herein for comparison with the available literatures to ascertain the  
115 reliability of the employed theoretical method. For the multi-generation OH  
116 oxidation reactions of styrene, all the possible pathways, including **H-abstraction**,  
117 **OH-addition**, O<sub>2</sub>-addition, cyclization, ring-opening, intramolecular H-shifts, **C-C**  
118 **bond and O-O bond scission**, and HO<sub>2</sub>-elimination, are taken into account.  
119 Additionally, the saturated concentrations of the formed highly oxidized products are  
120 estimated to identify the volatility classes.

## 121 **2. Computational methods**

### 122 **2.1 Electronic structures and energy calculations**

123 The electronic structures and energy calculations of all stationary points,  
124 including reactants (R), intermediates (IM), transition states (TS) and products (P), are  
125 performed using the Gaussian 16 program (Frisch et al., 2016). Geometric  
126 optimizations of all stationary points on the potential energy surfaces (PESs) are  
127 carried out at the M06-2X/6-31+g(d,p) level of theory, since it has reliable  
128 performance for describing the noncovalent interactions, thermochemical, and  
129 kinetics (Zhao and Truhlar, 2008). Harmonic vibrational frequencies are determined at  
130 the M06-2X/6-31+g(d,p) theoretical level to confirm the characteristics of all  
131 stationary points (a local minimum or a saddle point). The zero-point vibrational  
132 energy (ZPVE) is scaled by a factor of 0.967 (Alecú et al., 2010). Intrinsic reaction  
133 coordinate (IRC) calculations are carried out to ascertain the connection of the given  
134 TS between the designated local minima R and P (Fukui, 1981). Single point energy  
135 calculations are performed at the M06-2X/6-311++G(3df,3pd) level **based on the**  
136 **M06-2X/6-31+g(d,p) optimized geometries.**

137 **In order to further evaluate the reliability of the computational method employed**  
138 **herein, the single point energies of all the stationary points involved in the initial**  
139 **addition of OH radicals to styrene and intramolecular H-shift reactions of the first**  
140 **generation peroxy radicals S2-1-x are recalculated using the DLPNO-CCSD(T)/**  
141 **aug-cc-pVTZ method performed using the Orca 6.1 program (Neese, 2025). As shown**

142 in Table S1, the  $\Delta E_a$  values obtained using the M06-2X/6-311++G(3df,3pd) method  
143 are consistent with those derived from the DLPNO-CCSD(T)/aug-cc-pVTZ method.  
144 The largest deviation and the average absolute deviation are 1.2 and 0.6 kcal/mol,  
145 respectively, indicating that the computational method employed in this study is  
146 reliable. Considering the computational cost, the M06-2X/6-311++G(3df,3pd) method  
147 is employed to investigate the formation mechanism of highly oxidized products from  
148 the multi-generation OH oxidation of styrene. The energy barrier ( $\Delta E_a$ ) and reaction  
149 energy ( $\Delta E_r$ ) are defined as the difference in energy between TS and IM, as well as  
150 between P and R.

## 151 **2.2 Conformer search**

152 RO<sub>2</sub> radicals formed from the addition of O<sub>2</sub> to the carbon-centered site of alkyl  
153 radicals R have multiple possible conformers due to the different orientations of O<sub>2</sub>  
154 attack (Chen et al., 2021; Fu et al., 2020; Møller et al., 2016 and 2020). An initial  
155 structure of RO<sub>2</sub> radicals is optimized at the B3LYP/6-31+G(d) level and  
156 subsequently used as the starting geometry to perform the conformer search  
157 conducted using the Molclus program (Lu, 2024). The resulting structures are initially  
158 optimized at the B3LYP/6-31+G(d) level, as this method accurately predicts the  
159 relative energy ordering of different conformers (Møller et al., 2016 and 2020). For  
160 the intramolecular H-shift reactions of RO<sub>2</sub> radicals, the lengths of the O-O, C-H and  
161 O-H bonds in the conformational sampling of TSs are constrained to retain the cyclic  
162 TS structure. All unique conformers of R, TS and P within 5.0 kcal/mol with respect  
163 to the lowest energy conformer are further optimized at the M06-2X/6-31+g(d,p) level  
164 of theory. Then, the single point energy calculations are performed at the  
165 M06-2X/6-311++G(3df,3pd) level of theory. RO radicals formed by the bimolecular  
166 reactions of RO<sub>2</sub> radicals with HO<sub>2</sub> radicals and NO also have multiple conformers. In  
167 order to obtain the lowest energy conformer, a similar methodology is employed in  
168 the present study.

## 169 **2.3 Kinetics calculations**

170 The rate coefficients of unimolecular reactions, including intramolecular H-shifts,

171 cyclization, HO<sub>2</sub>-elimination, and C-C bond and C-O bond scissions, are calculated  
 172 using the RRKM theory along with energy-grained master equation (RRKM-ME)  
 173 (Holbrook et al., 1996). The rate coefficients of bimolecular reactions, involving  
 174 H-abstraction and OH-addition, are determined using the traditional transition state  
 175 theory (TST) (Fernández-Ramos et al., 2007). An asymmetric one-dimensional Eckart  
 176 model (Eckart, 1930) is employed to consider the tunneling correction factors in the  
 177 rate coefficient calculations based on RRKM-ME and TST. A single exponential down  
 178 model in the RRKM-ME calculations is utilized to approximate the collision transfer  
 179 ( $\langle \Delta E \rangle_{\text{down}} = 200 \text{ cm}^{-1}$ ). The Lennard-Jones parameters of all intermediate species are  
 180 estimated using the empirical formula as proposed by Gilbert and Smith (1990).

181 For the intramolecular H-shifts of RO<sub>2</sub> and RO radicals, the rate coefficients are  
 182 computed using the multiconformer transition state theory (MC-TST) (Møller et al.,  
 183 2016), which is expressed as Eq. (1): (Møller et al., 2016 and 2020; Pasik et al., 2024)

$$184 \quad k_{\text{MC-TST}} = \kappa \frac{k_{\text{B}}T}{h} \frac{\sum_i^{\text{TS conf.}} \exp\left(\frac{-\Delta E_i}{k_{\text{B}}T}\right) Q_{\text{TS},i}}{\sum_j^{\text{R conf.}} \exp\left(\frac{-\Delta E_j}{k_{\text{B}}T}\right) Q_{\text{R},j}} \exp\left(-\frac{E_{\text{TS}} - E_{\text{R}}}{k_{\text{B}}T}\right) \quad (1)$$

185 where  $\kappa$  is the Eckart tunneling coefficient,  $h$  is Planck's constant,  $k_{\text{B}}$  is  
 186 Boltzmann's constant, and  $T$  is the absolute temperature (298.15 K).  $Q_{\text{TS},i}$  and  $Q_{\text{R},j}$   
 187 refer to the partition functions of the corresponding transition state  $i$  and reactant  $j$   
 188 conformers, respectively.  $\Delta E_i$  and  $\Delta E_j$  represent the relative electronic energies  
 189 between the corresponding transition state  $i$  and reactant  $j$  conformers and the lowest  
 190 energy conformers, respectively.  $E_{\text{TS}}$  and  $E_{\text{R}}$  stand for the electronic energies of the  
 191 lowest energy transition state and reactant conformers, respectively. All kinetics  
 192 calculations are carried out using the KiSThelP 2021 and MESMER 6.0 programs  
 193 (Glowacki et al., 2012; Canneaux et al., 2013).

### 194 **3. Results and discussion**

#### 195 **3.1 First generation OH oxidation mechanisms of styrene**

196 Styrene is composed of a benzene ring and a vinyl group, and its oxidation  
 197 initiated by OH radicals may proceed either on the vinyl group or on the benzene ring.

198 Previous literature has demonstrated that the addition of OH radicals to terminal  
199 carbon ( $C_{\beta}$ -site) of a vinyl group in styrene is the dominant pathway, with the  
200 branching ratio of 88.2% (Wu et al., 2021). Therefore, the  $C_{\beta}$ -site OH-addition  
201 reaction is mainly considered in the present study. Figure 1 depicts that this reaction  
202 starts with the formation of a pre-reactive complex IM1, and then transforms into an  
203 alkyl radical S1-1 via transition state TS1 with a  $\Delta E_a$  of 0.8 kcal/mol. The rate  
204 coefficient of  $C_{\beta}$ -site OH-addition reaction is estimated to be  $1.5 \times 10^{-11} \text{ cm}^3$   
205  $\text{molecule}^{-1} \text{ s}^{-1}$  at ambient temperature, which is approximately consistent with the  
206 experimental ( $1.2\text{-}6.2 \times 10^{-11} \text{ cm}^3 \text{ molecule}^{-1} \text{ s}^{-1}$ ) and theoretical values ( $1.7\text{-}2.0 \times$   
207  $10^{-11} \text{ cm}^3 \text{ molecule}^{-1} \text{ s}^{-1}$ ) for the total rate coefficient of the reaction styrene + OH  
208 (Wu et al., 2021; Zhang et al., 2024).

209 Due to the existence of resonance structures with radical character on the  
210 aromatic ring, the resulting S1-1 can readily isomerize into three other species,  
211 namely, S1-2, S1-3 and S1-4. The attack of an  $O_2$  molecule on the C-center site of  
212 S1-1 leads to the formation of the first generation peroxy radicals S2-1-x ( $\Delta E_r > -59.6$   
213 kcal/mol). The formed S2-1-x includes eight energetically similar conformers due to  
214 the different orientations of  $O_2$  attack. In order to distinguish the different conformers,  
215 the subscript letter x is used in the present study. The energy ordering of different  
216 conformers follows an alphabetical sequence, in which letter a denotes the lowest  
217 energy conformer. The Boltzmann population of different conformers in S2-1-x is  
218 listed in Table S2.

219 For the unimolecular decomposition reactions of S2-1-x, there are three kinds of  
220 pathways. One is the intramolecular H-shift reactions, where the hydrogen atom  
221 migrates from the  $-CH_2$ ,  $-CH$  and  $-OH$  groups to the terminal oxygen atom of the  $-$   
222  $OO$  group leading to various alkyl and alkoxy radicals. Among these competing  
223 H-shift reactions, the hydrogen atom at the  $-OH$  group can be transferred via a  
224 six-membered ring transition state (1,5-H shift) to yield an alkoxy radical S3-1-a,  
225 which exhibits the lowest barrier ( $\Delta E_a = 21.0$  kcal/mol). The resulting S3-1-a can  
226 undergo the  $C_{\alpha}$ - $C_{\beta}$  bond cleavage to produce a formaldehyde and an alkyl radical  
227 S4-1-a ( $\Delta E_a = 0.8$  kcal/mol), followed by an OH radical release to form benzaldehyde

228 ( $\Delta E_a = 0.1$  kcal/mol). The rate coefficients for the aforementioned three pathways are  
229 calculated to be  $2.7 \times 10^{-4}$ ,  $4.6 \times 10^{10}$  and  $7.2 \times 10^{10}$  s<sup>-1</sup>, respectively. Based on the  
230 values of  $\Delta E_a$  and the corresponding rate coefficients, it can be concluded that the  
231 1,5-H shift reaction is the rate-determining step in the formation of benzaldehyde. The  
232 other is the cyclization, where the -OO group attacks the C=C double bond in the  
233 benzene ring forming a cyclic peroxide alkyl radical S3-1-c ( $\Delta E_a = 33.6$  kcal/mol).  
234 The last is the HO<sub>2</sub>-elimination, where a concerted process of C<sub>α</sub>-O and C<sub>β</sub>-H bonds  
235 scission forms a closed-shell species S3-1-b and a HO<sub>2</sub> radical byproduct ( $\Delta E_a = 33.3$   
236 kcal/mol). The aforementioned results show that the cyclization and HO<sub>2</sub>-elimination  
237 reactions are less important due to their higher barriers.

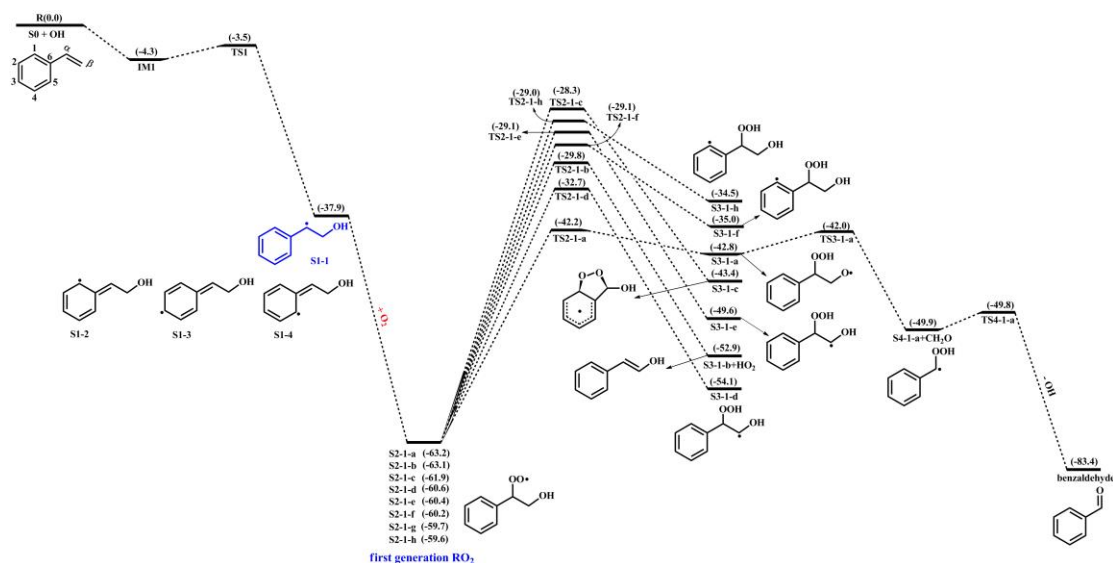
238 As depicted in Figure S1, the formations of the first generation peroxy radicals  
239 S2-2-x from the association reaction S1-2 + O<sub>2</sub> are strongly endothermic ( $\Delta E_r =$   
240 8.1-10.4 kcal/mol), suggesting that they have a significant potential to redissociate  
241 back to reactants S1-2 and O<sub>2</sub>. The resulting S2-2-x can undergo through various  
242 intramolecular H-shifts to yield distinct C-centered and O-centered radicals. Among  
243 these competing H-shift pathways, hydrogen transfer from the -OH group to the  
244 terminal oxygen of -OO group has the lowest barrier ( $\Delta E_a = 17.4$  kcal/mol). A similar  
245 conclusion is also obtained from the association reactions S1-3 + O<sub>2</sub> ( $\Delta E_r = 6.6-7.1$   
246 kcal/mol) and S1-4 + O<sub>2</sub> ( $\Delta E_r = 8.1-11.1$  kcal/mol) that the formations of the first  
247 generation peroxy radicals S2-3-x and S2-4-x are thermochemically unfavorable, and  
248 their subsequent intramolecular H-shift barriers are considerably high (Figures S2 and  
249 S3). Therefore, in the present study, we mainly focus on the subsequent reaction  
250 mechanisms of S2-1-x under both low and high NO<sub>x</sub> conditions.

251 In the low-NO<sub>x</sub> conditions, the bimolecular reaction with HO<sub>2</sub> radicals is  
252 expected to be the dominant sink for RO<sub>2</sub> radicals (Orlando and Tyndall, 2012;  
253 Vereecken et al., 2015). Previous studies have reported that the rate coefficient  
254  $k_{RO_2+HO_2}$  for the reactions of alkyl peroxy radicals with HO<sub>2</sub> radicals is  $1.7 \times 10^{-11}$   
255 cm<sup>3</sup> molecule<sup>-1</sup> s<sup>-1</sup> (Atkinson and Arey, 2003; Boyd et al., 2003). The typical  
256 atmospheric concentration of HO<sub>2</sub> radicals is 20-40 pptv (Wang et al., 2017; Bianchi  
257 et al., 2019), resulting in the pseudo-first-order rate constant  $k'_{RO_2+HO_2} = k_{RO_2+HO_2}$

258 [HO<sub>2</sub>] of 0.01-0.02 s<sup>-1</sup>. The isomerization reaction of RO<sub>2</sub> radicals is competitive with  
259 the bimolecular reactions with HO<sub>2</sub> radicals only when the rate coefficient of  
260 intramolecular H-shifts exceeds 0.01-0.02 s<sup>-1</sup>. In the high-NO<sub>x</sub> conditions, the  
261 bimolecular reaction of RO<sub>2</sub> radicals with NO is considered to be a dominant sink  
262 (Orlando and Tyndall, 2012; Vereecken et al., 2015). The rate coefficient  $k_{\text{RO}_2+\text{NO}}$  for  
263 the reaction of alkyl peroxy radicals with NO is determined to be  $9.0 \times 10^{-12} \text{ cm}^3$   
264  $\text{molecule}^{-1} \text{ s}^{-1}$  (Atkinson and Arey, 2003; Bianchi et al., 2019). The typical  
265 atmospheric concentration of NO is 0.4-40 ppbv (Wang et al., 2017; Wang et al.,  
266 2019), leading to the pseudo-first-order rate constant  $k'_{\text{RO}_2+\text{NO}} = k_{\text{RO}_2+\text{NO}} [\text{NO}]$  of  
267 0.1-10 s<sup>-1</sup>. The intramolecular H-shift reaction of RO<sub>2</sub> radicals can compete with the  
268 bimolecular reaction with NO only when the rate coefficient of the former case  
269 exceeds 10 s<sup>-1</sup>. Therefore, we use the  $k'_{\text{RO}_2+\text{HO}_2}$  (0.01-0.02 s<sup>-1</sup>) and  $k'_{\text{RO}_2+\text{NO}}$  (0.1-10 s<sup>-1</sup>)  
270 values as thresholds to evaluate the relative importance of the isomerization reactions  
271 of RO<sub>2</sub> radicals under the low- and high-NO<sub>x</sub> conditions. Previous studies have also  
272 employed the same methodology to evaluate the relative importance of isomerization  
273 and bimolecular reactions of RO<sub>2</sub> radicals during the OH-initiated oxidation of  
274 organophosphate esters and alkylbenzenes (Wang et al., 2017; Fu et al., 2024). For the  
275 intramolecular H-shift reactions of S2-1-x, the rate coefficient  $k_{\text{MC-TST}}$  is estimated to  
276 be  $1.6 \times 10^{-4} \text{ s}^{-1}$ , which is 2-4 orders of magnitude lower than  $k'_{\text{RO}_2+\text{HO}_2}$  and  $k'_{\text{RO}_2+\text{NO}}$ ,  
277 indicating that the isomerization reaction of S2-1-x is less competitive than the  
278 bimolecular reactions with HO<sub>2</sub> radicals and NO.

279 In the presence of NO, the bimolecular reactions of S2-1-x with NO initially  
280 proceed via oxygen-to-oxygen coupling to yield organic nitrites ROONO, which  
281 subsequently decompose into benzaldehyde and CH<sub>2</sub>OH radical or isomerize to  
282 organic nitrates RONO<sub>2</sub>. The energy barrier of the rate-limiting step predicted in  
283 Wang's study for the formation of benzaldehyde is 28.4 kcal/mol, which is  
284 approximately 4.0 kcal/mol greater than that for the formation of RONO<sub>2</sub> (Wang et al.,  
285 2015). In the absence of NO, the hydroperoxides ROOH formed from the bimolecular  
286 reaction of S2-1-x with HO<sub>2</sub> radicals are anticipated to be the dominate products. The  
287 aforementioned results are further confirmed by the recent smog chamber experiment

288 study that  $C_7$  and  $C_8$  series products, as well as organic nitrates are the main  
 289 components of SOA in the OH-initiated oxidation of styrene under different  $NO_x$   
 290 conditions (Yu et al., 2022). Considering that the extensive studies on the OH-initiated  
 291 oxidation of benzaldehyde have done (Sebbar et al., 2011; Zhao et al., 2022; Iuga et  
 292 al., 2008), this study primarily focuses on the multi-generation OH oxidation  
 293 mechanisms of ROOH and  $RONO_2$  under the low- and high- $NO_x$  conditions.



294  
 295 **Figure 1.** PES for the first-stage oxidation of styrene initiated by OH radicals and the  
 296 isomerization reactions of S2-1-x at the M06-2X/6-311++G(3df,3pd)//M06-2X/6-31+g(d,p) level

### 297 3.2 Second generation OH oxidation mechanisms of 1<sup>st</sup>-ROOH 298 and 1<sup>st</sup>-RONO<sub>2</sub>

299 The first generation products, including hydroperoxides 1<sup>st</sup>-ROOH and organic  
 300 nitrates 1<sup>st</sup>-RONO<sub>2</sub>, include multiple conformers. To obtain the global minimum of  
 301 1<sup>st</sup>-ROOH and 1<sup>st</sup>-RONO<sub>2</sub>, the conformer search is performed by using the Molclus  
 302 program. The resulting structures are initially optimized at the M06-2X/6-31+g(d,p)  
 303 level, then the single point energies are calculated at the M06-2X/6-311++G(3df,3pd)  
 304 level. The global minimum structures of 1<sup>st</sup>-ROOH (S4) and 1<sup>st</sup>-RONO<sub>2</sub> (S5) are  
 305 presented in Figure S4.

#### 306 3.2.1 The oxidation mechanism of 1<sup>st</sup>-ROOH initiated by OH 307 radicals

308 The reaction 1<sup>st</sup>-ROOH (S4) + OH proceeds through the addition of OH radicals

309 to either side of the benzene ring to yield various alkyl radicals, as depicted in Figure  
310 2. In the present study, *syn*-OH-addition is defined as the scenario in which the  
311 addition of OH radicals occurs at the same side as the –OOH group, while  
312 *anti*-OH-addition is referred to the scenario in which the addition of OH radicals  
313 occurs at the opposite side as the –OOH group. For the *syn*-OH-addition reactions, the  
314 addition of OH radicals to the C1-site of 1<sup>st</sup>-ROOH (S4) exhibits the lowest barrier  
315 ( $\Delta E_a = 3.6$  kcal/mol) due to the stability of the formed product, P<sub>S4-add1</sub>'. A similar  
316 conclusion is also obtained from the *anti*-OH-addition reactions that the OH-addition  
317 pathway occurring at the C1-site is favorable ( $\Delta E_a = 0.8$  kcal/mol). Notably, the  
318 preferred OH-addition pathway in the *anti*-OH-addition reactions exhibits greater  
319 competitiveness compared to that in the *syn*-OH-addition reactions. It can be  
320 explained by the greater steric hindrance present in the latter reaction. In order to  
321 further evaluate the reliability of our results,  $\Delta E_a$  of all the *syn*-OH-addition and  
322 *anti*-OH-addition reactions are recalculated using the DLPNO-CCSD(T)/  
323 aug-cc-pVTZ//M06-2X/6-311+G(d,p) method. As shown in Table S3, the  $\Delta E_a$  values  
324 obtained using the M06-2X/6-311++G(3df,3pd) method are in good agreement with  
325 those derived from the DLPNO-CCSD(T)/aug-cc-pVTZ method. The largest  
326 deviation and the average absolute deviation are 1.2 and 0.9 kcal/mol, respectively,  
327 indicating that the M06-2X/6-311++G(3df,3pd) method employed in this study is  
328 reliable. Based on the values of  $\Delta E_a$  obtained using the DLPNO-CCSD(T)/  
329 aug-cc-pVTZ method, it can also be concluded that the addition of OH radicals to  
330 C1-site, occurring at the opposite direction relative to the –OOH group, is  
331 energetically favorable. The rate coefficients of the addition of OH radicals to the  
332 different sites of 1<sup>st</sup>-ROOH are calculated to be  $8.2 \times 10^{-12}$  (C1-site),  $5.8 \times 10^{-15}$   
333 (C2-site),  $8.3 \times 10^{-15}$  (C3-site),  $8.6 \times 10^{-15}$  (C4-site),  $2.7 \times 10^{-12}$  (C5-site) and  $4.1 \times$   
334  $10^{-13}$  (C6-site) cm<sup>3</sup> molecule<sup>-1</sup> s<sup>-1</sup>, respectively. The branching ratios for OH addition  
335 to the C1, C5 and C6 sites are predicted to be 72.4%, 23.8% and 3.6%, respectively,  
336 while the sum of branching ratios for OH addition to other carbon sites is less than  
337 1%.

338 Our result is opposite to Zhang's finding that the addition of OH radicals to

339 C6-site would be the most favorable pathway (Zhang et al., 2024). The discrepancy  
340 can be explained by the following three factors: (1) The 1<sup>st</sup>-ROOH conformer selected  
341 in the Zhang's study is not the global minimum. In the present study, the global  
342 minimum conformer of 1<sup>st</sup>-ROOH, identified through the conformer search, is found  
343 to be 2.2 kcal/mol lower than the 1<sup>st</sup>-ROOH structure selected in the Zhang's study. (2)  
344 The pre-reactive complexes are not considered in the Zhang's study. The addition of  
345 OH radicals to C1-, C2-, C3- and C6-sites, occurring at the opposite direction relative  
346 to the -OOH group, are merely considered in the Zhang's study. They found that the  
347 apparent energy barrier of the addition of OH radicals to C6-site is smallest, and is  
348 therefore expected to be the favorable pathway. Actually, these OH-addition reactions  
349 are modulated by the pre-reactive complexes. It may be inappropriate to determine the  
350 favorable pathway based solely on apparent activation energy without considering the  
351 pre-reaction complexes. (3) From a geometric perspective, the addition of OH radicals  
352 to C6-site is associated with greater steric hindrance compared to other sites, as  
353 C6-atom connects with a larger functional group. Base on the aforementioned  
354 discussions, we believe that the addition of OH radicals to C6-site is unlikely to be the  
355 dominant pathway. Our calculations also confirm that the addition of OH radicals to  
356 C6-site is less importance compared to that at the C1-site.

357 Our conclusion is further supported by the reaction toluene + OH that the  
358 *ortho*-OH-addition reaction exhibits significant dominance, with the branching ratio  
359 of up to 69.8-75.8% (Ji et al., 2017; Zhang 2019; Wu et al., 2020). Considering the  
360 high reactivity of *ortho*-OH-addition in the reactions toluene + OH and 1<sup>st</sup>-ROOH  
361 (S4) + OH, the substitute effects of the -CH<sub>3</sub> and -OOH groups are explicitly  
362 discussed in the present study. Notably, the -CH<sub>3</sub> group in toluene is bonded to the C6  
363 atom, and the -OOH group in 1<sup>st</sup>-ROOH is bonded to the C $\alpha$  atom, as depicted in  
364 Figure S5. The optimized geometries of toluene and 1<sup>st</sup>-ROOH and the NPA atomic  
365 charges of all the carbon atoms in the benzene ring are displayed in Figure S5. The  
366 C-C bond lengths and the C-C-C bond angles in the benzene ring of toluene are  
367 approximately 1.39 Å and 120°, respectively, which are consistent with those in the  
368 benzene ring of 1<sup>st</sup>-ROOH. The aforementioned results show the effect of the -CH<sub>3</sub>

369 and –OOH groups on the geometric structure of benzene ring is negligible. From the  
370 perspective of NPA atomic charges, the charges on the C1 (-0.246 e) and C5 (-0.246 e)  
371 atoms are more greater than those on the other carbon atoms in the benzene ring of  
372 toluene. And the OH-adduct formed from the *ortho*-OH-addition reaction exhibits the  
373 greater stability. These results indicate that the –CH<sub>3</sub> group is a typical *ortho*-directing  
374 substituent and exerts an activating effect on the *ortho*-site of the benzene ring, which  
375 explains why the *ortho*-OH-addition reaction is predominant in the reaction toluene  
376 + OH. Compared with the charges on the carbon atoms in the benzene ring of toluene,  
377 the charges on C1 and C6 atoms increase by 0.013 e and 0.057 e, respectively, in  
378 1<sup>st</sup>-ROOH, which can be attributed to the electron-withdrawing effect of the –OOH  
379 group. The charge on the C1 atom (-0.259 e) is the highest, and the stability of the  
380 resulting OH-adduct is the greatest, implying that the addition of OH radicals to  
381 C1-site is dominant in the reaction 1<sup>st</sup>-ROOH + OH. Therefore, a direct comparison  
382 of the favorable OH-addition pathway in the reactions toluene + OH and 1<sup>st</sup>-ROOH  
383 (S4) + OH is performed in this study.

384 The formed product P<sub>S4-add1</sub> includes two conjugate double bonds (C<sub>2</sub>=C<sub>3</sub> and  
385 C<sub>4</sub>=C<sub>5</sub>), which can readily isomerize to P<sub>S4-add2</sub> and P<sub>S4-add3</sub>, as evident from Figure S6.  
386 In the present of O<sub>2</sub>, the attack of an O<sub>2</sub> molecule on the C-centered site of P<sub>S4-add1</sub>,  
387 P<sub>S4-add2</sub>, and P<sub>S4-add3</sub> proceed via the barrierless processes to produce the second  
388 generation peroxy radicals P<sub>S4-add1-a/-s</sub>, P<sub>S4-add2-a/-s</sub> and P<sub>S4-add3-a/-s</sub>. The O<sub>2</sub>-addition  
389 reaction occurring at the same direction as the –OOH group is defined as  
390 *syn*-O<sub>2</sub>-addition, while the O<sub>2</sub>-addition reaction occurring at the opposite direction as  
391 the –OOH group is defined as *anti*-O<sub>2</sub>-addition. For the reaction P<sub>S4-add1</sub> + O<sub>2</sub> →  
392 P<sub>S4-add1-a/-s</sub>, ΔE<sub>r</sub> of *anti*-O<sub>2</sub>-addition is -5.8 kcal/mol, which is lower than that of  
393 *syn*-O<sub>2</sub>-addition by 0.4 kcal/mol, suggesting that *anti*-O<sub>2</sub>-addition is preferable over  
394 *syn*-O<sub>2</sub>-addition in energy. For the reactions P<sub>S4-add2</sub> + O<sub>2</sub> → P<sub>S4-add2-a/-s</sub> and P<sub>S4-add3</sub> +  
395 O<sub>2</sub> → P<sub>S4-add3-a/-s</sub>, it can be concluded the same by the ΔE<sub>r</sub> values that  
396 *anti*-O<sub>2</sub>-addition reaction is energetically feasible.

397 The resulting P<sub>S4-add1-a/-s</sub> can proceed intramolecular cyclization reaction, where  
398 the attack of end-site oxygen atom of the –OO group on C2-site of the C<sub>2</sub>=C<sub>3</sub> double

399 bond, leading to the formation of peroxide bicyclic alkyl radicals.  $\Delta E_a$  and  $\Delta E_r$  of the  
400 reaction  $P_{S4-add1-a} \rightarrow P_{S4-add1-a-1}$  are 11.8 and -16.8 kcal/mol, respectively, which are  
401 lower than those of the reaction  $P_{S4-add1-s} \rightarrow P_{S4-add1-s-1}$  by 3.9 and 2.2 kcal/mol,  
402 respectively. The aforementioned results reveal that the intramolecular cyclization  
403 reaction of *anti*-O<sub>2</sub>-addition product  $P_{S4-add1-a}$  is favorable on both thermochemically  
404 and kinetically. A similar conclusion is also derived from the intramolecular  
405 cyclization reactions of *anti*-O<sub>2</sub>-addition products  $P_{S4-add2-a}$  and  $P_{S4-add3-a}$ . Notably, the  
406 barriers of the intramolecular cyclization reactions  $P_{S4-add2-a} \rightarrow P_{S4-add2-a-1}$  ( $\Delta E_a =$   
407 31.1 kcal/mol) and  $P_{S4-add2-a} \rightarrow P_{S4-add2-a-2}$  ( $\Delta E_a = 34.6$  kcal/mol) are extremely high,  
408 making them insignificant in the atmosphere. The tautomerization between  
409  $P_{S4-add1-a-1}$  and  $P_{S4-add3-a-1}$  readily occurs due to the existence of resonance structures,  
410 and it is therefore that the latter conformer is selected as a prototype for the  
411 investigating of its subsequent reaction mechanism.

412 The formed  $P_{S4-add3-a-1}$  can combine with an O<sub>2</sub> molecule leading to the third  
413 generation peroxy radicals (also called as peroxide bicyclic peroxy radicals, BPR)  
414  $P_{S4-add3-a-2}$ , and the lowest energy conformer is presented in Figure S7. The  
415 isomerization of  $P_{S4-add3-a-2}$  may undergo through a concerted process of the cleavage  
416 of -O-O- bridge bond and C<sub>1</sub>-C<sub>2</sub> bond as well as hydrogen atom transfer from the  
417 hydroxyl group to the bridge oxygen atom, yielding a new peroxy radical ( $\Delta E_a = 28.5$   
418 kcal/mol). The room temperature rate coefficient is calculated to be  $3.0 \times 10^{-9} \text{ s}^{-1}$ ,  
419 which is several orders of magnitude low than the typical pseudo-first-order rate  
420 constants  $k'_{RO_2+HO_2}$  (0.01-0.02 s<sup>-1</sup>) and  $k'_{RO_2+NO}$  (0.1-10 s<sup>-1</sup>), suggesting that the  
421 isomerization reaction is less importance in the atmosphere. Therefore, the  
422 bimolecular reactions of  $P_{S4-add3-a-2}$  with HO<sub>2</sub> radicals with NO are mainly taken into  
423 consideration in this study.

424 In the pristine environments,  $P_{S4-add3-a-2}$  can react with HO<sub>2</sub> radicals resulting in  
425 the formation of the second generation products, bicyclic hydroperoxide 2<sup>nd</sup>-ROOH  
426 (S6) and peroxide bicyclic alkoxy radical (BAR)  $P_{S4-add3-a-3}$ , as depicted in Figure S7.  
427 For the subsequent reactions of S6 initiated by OH radicals, the detailed mechanisms  
428 are discussed in Section 3.3.1. From Figure 3, it can be seen that the unimolecular

429 decomposition of  $P_{S4-add3-a-3}$  involves two kinds of pathways. One is the ring-opening  
430 reaction, where the breakage of  $C_5-C_6$  bond produces an alkyl radical  $S7$  ( $\Delta E_a = 5.9$   
431 kcal/mol.). The other is cyclization reaction, where the attack of oxygen atom of  
432 O-centered site on the C4-site of the  $C_3=C_4$  double bond generates the ring-retaining  
433 alkyl radical  $S15$  ( $E_a = 8.0$  kcal/mol). The branching ratios for the formation of  $S7$  and  
434  $S15$  are predicted to be 74.7% and 25.3%, respectively.

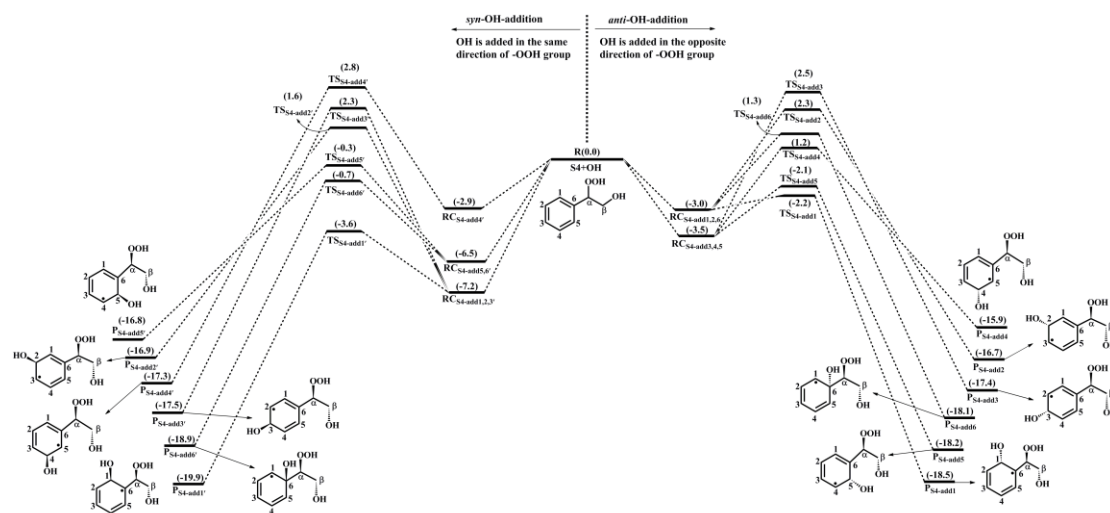
435 As shown in Figure 3,  $S7$  decomposes through the barrierless rupture of -O-O-  
436 bridge bond to form alkoxy radical  $S8-x$ , which includes five possible conformers as  
437 presented in Figure S8. The Boltzmann populations of different conformers are listed  
438 in Table S4.  $S8-x$  can undergo various intramolecular H-shifts, in which a hydrogen  
439 atom is transferred from different carbon atoms to O-centered site, forming the alkyl  
440 radicals. Among the competing H-shift reactions, 1,5 H-shift occurring at the -  
441  $C_5(O)H$  group exhibits the smallest barrier ( $\Delta E_a = 0.6$  kcal/mol), and  $k_{MC-TST}$  is  
442 calculated to be  $8.2 \times 10^9$  s<sup>-1</sup> at ambient temperature (Table S5). The formed  $S8-c-P$   
443 can readily isomerize to  $S9$  due to its resonance stabilized structure. The unimolecular  
444 decomposition of  $S9$  can proceed through the C1-C2 bond scission to produce a  
445 ketene-enol  $S10$  and an alkyl radical  $S10-1$  ( $\Delta E_a = 16.1$  kcal/mol), followed by  
446 reaction with  $O_2$  leading to a  $HO_2$  radical and a 1,2-dicarbonyl compound  $S10-2$  ( $\Delta E_a$   
447 = 14.0 kcal/mol). Alternatively,  $S9$  may undergo via the elimination of CO to generate  
448 an alkyl radicals  $S11$  ( $\Delta E_a = 29.4$  kcal/mol). The aforementioned results show that the  
449 formation of  $S10$  and  $S10-1$  is energetically favorable, with the rate coefficient  $k_{S10}$  of  
450 26.1 s<sup>-1</sup>.

451 In the presence of  $O_2$ , the attack of an  $O_2$  molecule on the C-centered sites of  $S9$   
452 leads to the fourth generation peroxy radical  $S12-x$  ( $\Delta E_r > -20.5$  kcal/mol). Adopting  
453 the rate coefficient  $k_{R+O_2}$  of  $6.0 \times 10^{-12}$  cm<sup>3</sup> molecule<sup>-1</sup> s<sup>-1</sup> for the reactions of alkyl  
454 radicals with  $O_2$ , and the atmospheric  $O_2$  concentration of  $5 \times 10^{18}$  molecule cm<sup>-3</sup> (Ma  
455 et al., 2021), the pseudo-first-order rate constant  $k'_{R+O_2} = k_{R+O_2} [O_2]$  is  $3.0 \times 10^7$  s<sup>-1</sup>.  
456 The unimolecular decomposition of alkyl radicals is competitive only when their  
457 decay rate exceeds  $3.0 \times 10^7$  s<sup>-1</sup>.  $k'_{R+O_2}$  is about six orders of magnitude greater than  
458  $k_{S10}$ , indicating that the unimolecular decomposition of  $S9$  is less importance. As

459 shown in Figure S9, S12-x can proceed various intramolecular H-shift reactions,  
460 where hydrogen atom migrates from the different carbon sites or hydroxyl groups to  
461 the terminal oxygen atom of the -OO group, resulting in the formation of QOOH  
462 radicals and alkoxy radicals. Among these competing H-shift reactions, the 1,7-H  
463 transfer at the C $\alpha$ -site leading to the formation of S12-d-P exhibits the smallest barrier  
464 ( $\Delta E_a = 17.4$  kcal/mol). Then, it decomposes to yield an OH radical and a closed-shell  
465 product S13 containing a hydroperoxide, three hydroxyl and three carbonyl groups  
466 ( $\Delta E_a = 1.1$  kcal/mol).

467 S8-x can proceed through the C<sub>1</sub>-C<sub>2</sub> bond scission to yield an unsaturated  
468 1,4-dicarbonyl species S14 and an alkyl radical S10-1 ( $\Delta E_a = 2.2$  kcal/mol), with the  
469 rate coefficient of  $2.1 \times 10^{10}$  s<sup>-1</sup>. Notably, both the 1,5 aldehyde H-shift and C<sub>1</sub>-C<sub>2</sub>  
470 bond scission reactions yield a closed-shell species S10-2 with up to five oxygen  
471 atoms, and the branching ratios are predicted to be 28.1% and 71.9%, respectively.  
472 The result is further supported by the previous study that the proportion of aldehyde  
473 H-shift products constitutes about one third of the total products in the reaction  
474 benzene + OH (Wang et al., 2020).

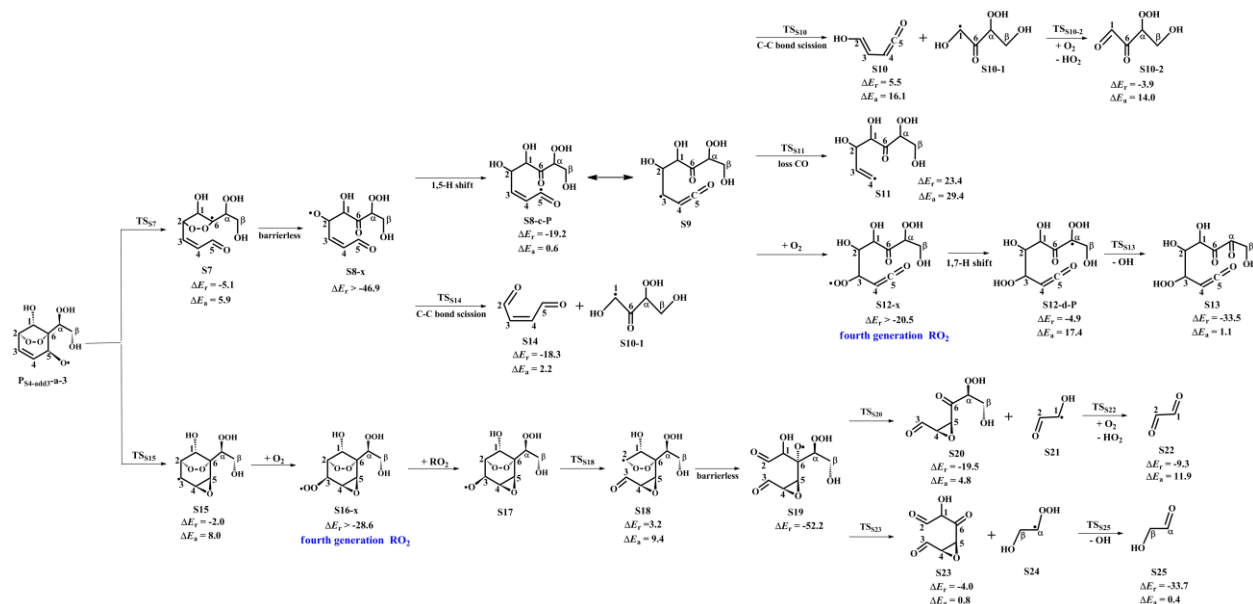
475 As shown in Figure 3, S15 can further react with O<sub>2</sub> leading to the fourth  
476 generation peroxy radical S16-x, which can proceed either intramolecular H-shifts  
477 forming QOOH radicals (Figure S10), or reactions with RO<sub>2</sub> radicals and NO forming  
478 alkoxy radical S17. Notably, the barriers of intramolecular H-shifts are extremely  
479 high ( $\Delta E_a > 34.6$  kcal/mol), making them less importance in the atmosphere. The  
480 transformation of S17 undergoes through the breakage of C<sub>2</sub>-C<sub>3</sub> bond to produce an  
481 alkyl radical S18 ( $\Delta E_a = 9.4$  kcal/mol), followed by fragmentation into an alkoxy  
482 radical S19 via the barrierless rupture of the -O-O- bridge bond. Then, S19 dissociates  
483 to an OH radical, a glycolaldehyde S25 and a C<sub>6</sub>-epoxide product S23 bearing a  
484 hydroxy and three carbonyl groups, being the dominant pathway. The regeneration of  
485 OH radicals drives the successive autoxidation of styrene, eventually leading to the  
486 formation of the highly oxidized products.



487

488 **Figure 2.** PES for the oxidation of 1<sup>st</sup>-ROOH(S4) initiated by OH radicals at the  
 489 M06-2X/6-311++G(3df,3pd)//M06-2X/6-31+g(d,p) level

490



491

492 **Figure 3.** PES for the unimolecular decomposition of P<sub>S4-add3-a-3</sub> and its subsequent reactions at  
 493 the M06-2X/6-311++G(3df,3pd)//M06-2X/6-31+g(d,p) level

### 494 3.2.2 The oxidation mechanism of 1<sup>st</sup>-RONO<sub>2</sub> initiated by OH

#### 495 radicals

496 The OH-initiated oxidation of 1<sup>st</sup>-RONO<sub>2</sub> (S5) proceeds through the addition of  
 497 OH radicals to different carbon sites in the benzene ring to form various alkyl radicals  
 498 P<sub>S5-addx</sub>, as depicted in Figure 4. Among the competing OH-addition reactions, the  
 499 OH-addition reaction at the C1-site, which proceeds on the opposite direction as the –  
 500 ONO<sub>2</sub> group, has the smallest barrier (R<sub>S5-add1</sub>, ΔE<sub>a</sub> = 0.4 kcal/mol) due to the stability

501 of the formed product  $P_{S5-add1}$ . The result again shows that the *ortho*-addition reaction  
502 is energetically feasible.  $P_{S5-add1}$  may isomerize to two other resonance structures,  
503 namely,  $P_{S5-add2}$  and  $P_{S5-add3}$ . For the reaction  $P_{S5-add1} + O_2$ ,  $O_2$  may add on either the  
504 opposite (*anti*- $O_2$ -addition) or the same direction (*syn*- $O_2$ -addition) relative to the –  
505  $NO_3$  group, leading to the second generation peroxy radicals  $P_{S5-add1-a}$  and  $P_{S5-add1-s}$   
506 (Figure S11). The exoergicity of these two reactions are -6.7 and -4.4 kcal/mol,  
507 respectively, suggesting that the *anti*- $O_2$ -addition reaction is thermochemically  
508 favorable. Next, they can isomerize via a cyclization process to yield  $P_{S5-add1-a-1}$  and  
509  $P_{S5-add1-s-1}$  with the  $\Delta E_a$  of 13.3 and 18.1 kcal/mol. This result shows that the  
510 cyclization reaction of *anti*- $O_2$ -addition product  $P_{S5-add1-a}$  is kinetically feasible. A  
511 similar conclusion is also obtained from the reaction  $P_{S5-add3} + O_2$  that the formation of  
512 *anti*- $O_2$ -addition product  $P_{S5-add3-a-1}$  is dominant. Due to the existence of the  
513 conjugate double bond, it facilitates the tautomerization between  $P_{S5-add1-a-1}$  and  
514  $P_{S5-add3-a-1}$ . Therefore, we mainly focus on the subsequent chemistry of  $P_{S5-add3-a-1}$  in  
515 the present study.

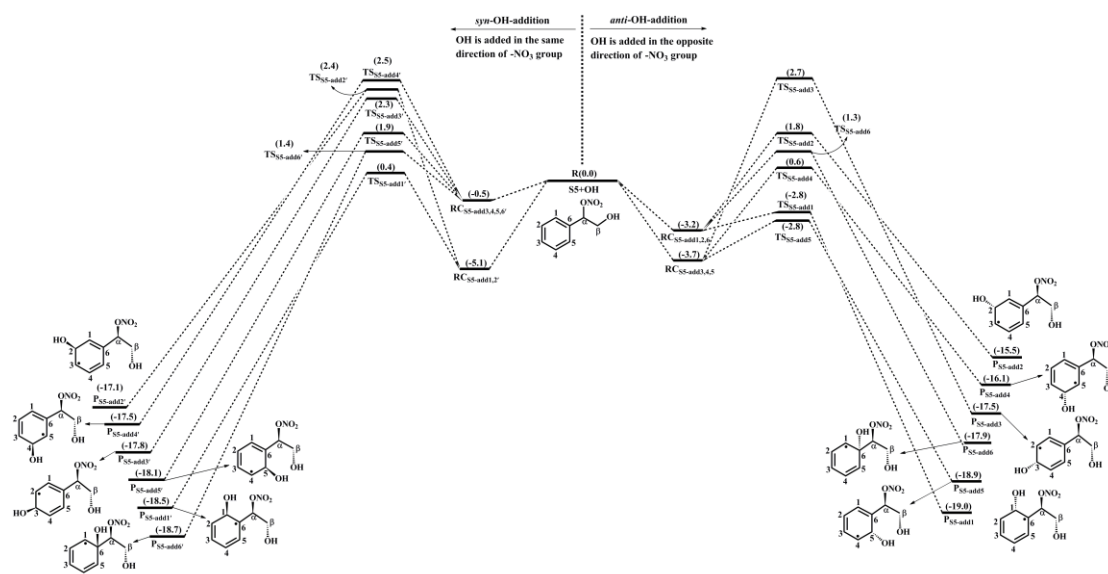
516  $P_{S5-add3-a-1}$  can further react with an  $O_2$  molecule leading to the third generation  
517 peroxy radicals  $P_{S5-add3-a-2}$ , which include multiple conformers. The lowest energy  
518 conformer resulting from conformer search is presented in Figure S12. In urban  
519 environments, the bimolecular reaction of  $P_{S5-add3-a-2}$  with NO yields the second  
520 generation products, a bicyclic organic nitrate 2<sup>nd</sup>-RONO<sub>2</sub> (S26) and a BAR  
521  $P_{S5-add3-a-3}$ , as displayed in Figure S12. The detailed mechanism of OH-initiated  
522 oxidation of S26 is discussed in Section 3.3.2. As shown in Figure 5,  $P_{S5-add3-a-3}$  can  
523 either proceed via a ring opening process to form an alkyl radical S27 ( $\Delta E_a = 7.3$   
524 kcal/mol), or undergo through a cyclization process to generate an epoxide species  
525 S35 ( $\Delta E_a = 8.5$  kcal/mol). The branching ratios of these two reactions are predicted to  
526 be 69.2% and 30.8%, respectively. Notably, the branching ratio of cyclization reaction  
527 of  $P_{S5-add3-a-3}$  increases by 5.5% compared to that of cyclization reaction of  
528  $P_{S4-add3-a-3}$ , suggesting that the  $-ONO_2$  substitution is beneficial to cyclization  
529 reaction.

530 The degradation of S27 proceeds through the barrierless scission of -O-O- bridge  
531 bond to form S28-x, and the Boltzmann populations of different conformers are listed  
532 in Table S6. S28-x can undergo via various intramolecular H-shifts to produce QOOH  
533 radicals, in which hydrogen atom transfer from the -C(O)H group to the terminal  
534 oxygen atom of the -OO group forming S28-e-P has the smallest barrier ( $\Delta E_a = 2.0$   
535 kcal/mol) (Figure S13). S28-e-P can readily isomerize to S29, which includes two  
536 distinct decomposition pathways. One is the C1-C2 bond cleavage, yielding a  
537 ketene-enol S30 and an alkyl radical S30-1 ( $\Delta E_a = 17.8$  kcal/mol), followed by  
538 reaction with O<sub>2</sub> to form a HO<sub>2</sub> radical and a 1,2-dicarbonyl species S30-2 ( $\Delta E_a =$   
539 11.7 kcal/mol). The other is the elimination of CO to generate an alkyl radical S31  
540 ( $\Delta E_a = 24.8$  kcal/mol), but the barrier is considerably high, making this pathway less  
541 competitive. The rate coefficient for the formation of S30 and S30-1 is calculated to  
542 be 14.4 s<sup>-1</sup>, which is about six orders of magnitude lower than the pseudo-first-order  
543 rate constant  $k'_{R+O_2}$ , indicating that the unimolecular decomposition of S29 is  
544 insignificant.

545 In the presence of O<sub>2</sub>, the bimolecular reaction of S29 with O<sub>2</sub> produces the  
546 fourth generation peroxy radicals S32-x, comprising five energetically similar  
547 conformers as shown in Figure S14. For the 1,7-H transfer reaction, hydrogen atom at  
548 the C $\alpha$ -site can be transferred through an eight-membered ring transition state to  
549 generate an alkyl radical S32-d-P ( $\Delta E_a = 23.3$  kcal/mol), followed by the elimination  
550 of NO<sub>2</sub> forming a closed product S33 ( $\Delta E_a = 1.0$  kcal/mol). S33 and S13 are isomeric  
551 species, with the former exhibiting more stability than the latter. S28-x can proceed  
552 through the cleavage of C<sub>1</sub>-C<sub>2</sub> bond to generate an unsaturated 1,4-dicarbonyl  
553 compound S34 and an alkyl radical S30-1. The rare coefficients of the 1,5 aldehyde  
554 H-shift and C1-C2 bond scission reactions are predicted to be  $1.7 \times 10^9$  and  $5.8 \times 10^9$   
555 s<sup>-1</sup> (Table S7), respectively, with the branching ratios of 23% and 77%. S30-1, formed  
556 from the above mentioned two pathways, may undergo through H-abstraction by O<sub>2</sub>  
557 to yield an organic nitrate S30-2 bearing a hydroxyl and two carbonyl groups ( $\Delta E_a =$   
558 11.7 kcal/mol).

559 S35 can combine with an O<sub>2</sub> molecule forming the fourth generation peroxy

560 radicals S36-x, which have five possible conformers as shown in Figure S15. S36-x  
 561 can proceed either intramolecular H-shifts forming QOOH radicals, or reaction with  
 562 RO<sub>2</sub> radicals and NO generating alkoxy radical S37. However, the barriers of  
 563 intramolecular H-shifts are extremely high ( $\Delta E_a > 31.3$  kcal/mol), making them less  
 564 importance in the atmosphere. The degradation of S37 initially proceeds via the  
 565 breakage of C<sub>2</sub>-C<sub>3</sub> bond to form S38 ( $\Delta E_a = 9.2$  kcal/mol), followed by decomposition  
 566 into an alkoxy radical S39 via the barrierless scission of -O-O- bridge bond. The  
 567 dominant pathway of the unimolecular decomposition of S39 is the formation of a  
 568 glyoxal and a C<sub>6</sub>-epoxide species S40-1 bearing a -NO<sub>3</sub>, a hydroxyl and two carbonyl  
 569 groups. This process differs from the unimolecular decay of S19, where the favorable  
 570 pathways is the formation of a tricarbonyl compound S23. The aforementioned results  
 571 reveal that the preferable pathway is strongly dependent on the breakage of C-C bond  
 572 associated with the property of substituents in the decomposition of alkoxy radicals.



573  
 574 **Figure 4.** PES for the oxidation of 1<sup>st</sup>-RONO<sub>2</sub>(S5) initiated by OH radicals at the  
 575 M06-2X/6-311++G(3df,3pd)//M06-2X/6-31+g(d,p) level

576  
 577

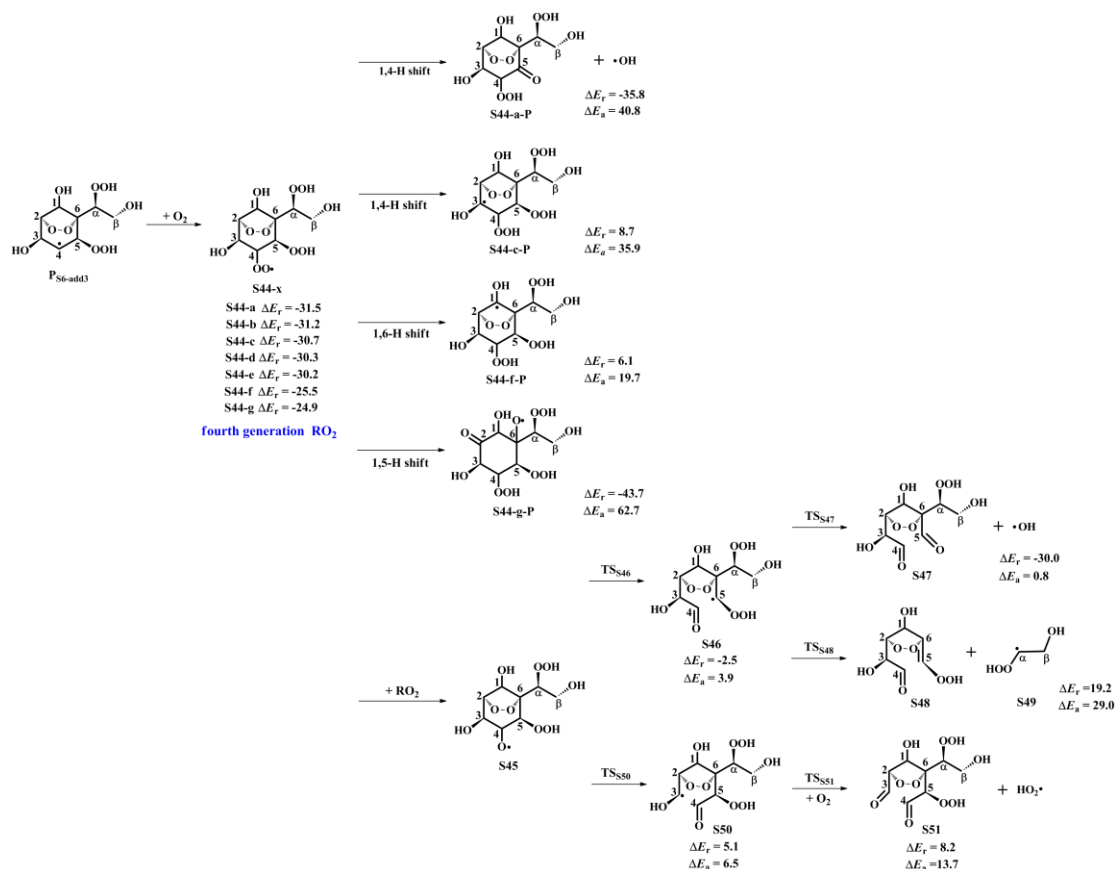


609 favorable pathway ( $\Delta E_a = 3.6$  kcal/mol) and the exoergicity of -20.2 kcal/mol. It is  
600 mainly because that the presence of an allyl group enhances the stability of the  
601 resulting product  $P_{S6-abs5}$ . Notably, the abstraction of hydrogen atom at the C2-site  
602 proceeds through a concerted process of C<sub>2</sub>-H bond and -O-O- bridge bond rupture,  
603 leading to the formation of an alkoxy radical  $P_{S6-abs2}$  ( $\Delta E_a = 7.2$  kcal/mol). This  
604 reaction is expected to be less importance due to its higher energy barrier. The rate  
605 coefficient of the favorable OH-addition reaction is calculated to be  $6.4 \times 10^{-11}$  cm<sup>3</sup>  
606 molecule<sup>-1</sup> s<sup>-1</sup>, which is about one order of magnitude greater than that of the  
607 preferable H-abstraction reaction ( $4.1 \times 10^{-12}$  cm<sup>3</sup> molecule<sup>-1</sup> s<sup>-1</sup>). Based on the above  
608 discussion, it can be concluded that OH-addition reaction is favorable on both  
609 thermochemically and kinetically. This conclusion is further supported by the OH +  
610 alkene reaction systems that OH-addition pathways are predominant (Chen et al.,  
611 2021; Yang et al., 2017; Arathala and Musah, 2024).

612 As depicted in Figure S18, the unimolecular decay of the product  $P_{S6-add3}$   
613 resulting from the favorable OH-addition reaction proceeds through a cyclization  
614 process to yield an epoxide compound S41 and an OH radical byproduct with the  $\Delta E_a$   
615 of 15.3 kcal/mol and the rate coefficient  $k_{R41}$  of  $1.8 \times 10^2$  s<sup>-1</sup>, or undergoes via  
616 intramolecular 1,4 H-shift to form a peroxy radical S42 with the  $\Delta E_a$  of 21.8 kcal/mol  
617 and the rate coefficient  $k_{R43}$  of  $1.9$  s<sup>-1</sup>, or proceeds via the elimination of hydrogen  
618 atom to produce an alkene S43 with the  $\Delta E_a$  of 37.9 kcal/mol. Based on the values of  
619  $\Delta E_a$  and the corresponding rate coefficients, the dominant pathway of the  
620 unimolecular decomposition of  $P_{S6-add3}$  is the formation of S41. In the presence of O<sub>2</sub>,  
621 the pseudo-first-order rate constant  $k'_{R+O_2}$  of the reactions of alkyl radicals with O<sub>2</sub> is  
622  $3.0 \times 10^7$  s<sup>-1</sup>, which is about five orders of magnitude greater than  $k_{R41}$ , suggesting  
623 that the unimolecular decomposition of  $P_{S6-add3}$  is insignificant.

624 As shown in Figure 6, the fourth generation peroxy radicals S44-x formed in the  
625 addition reaction  $P_{S6-add3} + O_2$  can either proceed via intramolecular H-shifts to form  
626 QOOH, or undergo through self- or cross-reactions to yield an alkoxy radical S45.  
627 Due to the considerably high barriers of intramolecular H-shifts, they are deemed to  
628 be negligible under atmospheric conditions. S45 can convert into an alkyl radical S46

629 through the cleavage of C<sub>4</sub>-C<sub>5</sub> bond, or dissociate to an alkyl radical S50 via the  
 630 rupture of C<sub>3</sub>-C<sub>4</sub> bond. The barrier of the former reaction is 3.9 kcal/mol, which is  
 631 lower than that of the latter pathway by 2.6 kcal/mol, indicating that the formation of  
 632 S46 is kinetically preferable. Then, S46 decomposes into an OH radical byproduct  
 633 and a C<sub>8</sub>-product S47 bearing a –OOH, a peroxide bridge, two carbonyls, and three  
 634 hydroxy groups, which is expected to be the dominant pathway owing to its lower  
 635 barrier. The rate coefficient  $k_{RS47}$  is estimated to be  $1.8 \times 10^9 \text{ s}^{-1}$ , which is about two  
 636 orders of magnitude greater than the pseudo-first-order rate constant  $k'_{R+O_2}$  ( $3.0 \times 10^7$   
 637  $\text{s}^{-1}$ ). The result reveals that the unimolecular decomposition of S46 is more  
 638 competitive than the bimolecular reaction with O<sub>2</sub>. The formed OH radicals can once  
 639 again participate in the oxidations of styrene and its highly oxidized products,  
 640 continuing these processes until they are completely consumed.



641  
 642 **Figure 6.** PES for the subsequent reactions of P<sub>S6-add3</sub> in the presence of O<sub>2</sub> at the  
 643 M06-2X/6-311++G(3df,3pd)//M06-2X/6-31+g(d,p) level

644 **3.3.2 The oxidation mechanism of 2<sup>nd</sup>-RONO<sub>2</sub> initiated by OH**  
 645 **radicals**

646 OH-initiated oxidation of 2<sup>nd</sup>-RONO<sub>2</sub> (S26) includes four different OH-addition  
647 pathways and five different H-abstraction pathways, as displayed in Figures S19 and  
648 S20. For the OH-addition reactions, the attack of OH radicals on the C3-site of the  
649 C<sub>3</sub>=C<sub>4</sub> double bond forming the product P<sub>S26-add3</sub>, occurring on the same direction  
650 relative to the -ONO<sub>2</sub> group, is found to be the favorable pathway ( $\Delta E_a = 2.4$   
651 kcal/mol,  $\Delta E_r = -33.6$  kcal/mol). For the H-abstraction reactions, the abstraction of  
652 hydrogen atom at the C5-site is identified as the preferable pathway ( $\Delta E_a = 5.7$   
653 kcal/mol,  $\Delta E_r = -20.1$  kcal/mol) due to the enhanced stability of the resulting product  
654 P<sub>S26-add5</sub> by the presence of an allyl group. By comparing the values of  $\Delta E_a$  and  $\Delta E_r$  of  
655 the favorable OH-addition and H-abstraction pathways, it can be concluded that the  
656 former case is dominant on both thermochemically and kinetically. This conclusion is  
657 consistent with the result from the reaction 2<sup>nd</sup>-ROOH (S6) + OH that OH-addition is  
658 more competitive than H-abstraction.

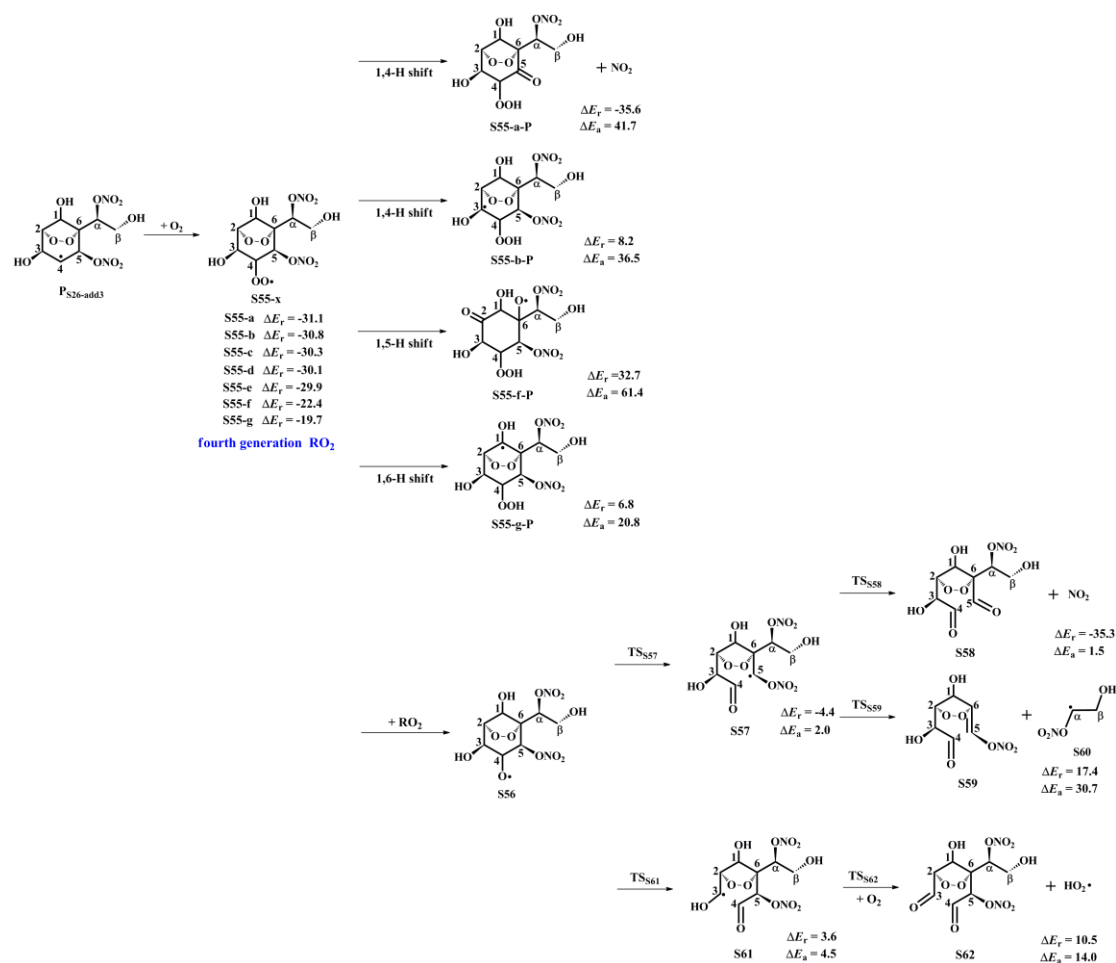
659 The product P<sub>S26-add3</sub> arising from the favorable OH-addition pathway has three  
660 potential unimolecular decay pathways, as depicted in Figure S21: (1) P<sub>S26-add3</sub>  
661 dissociates to an epoxide S52 and a NO<sub>2</sub> molecule through a cyclization process with  
662 the  $\Delta E_a$  of 18.5 kcal/mol and the rate coefficient  $k_{R52}$  of 0.4 s<sup>-1</sup>; (2) P<sub>S26-add3</sub> isomerizes  
663 to an alkyl radical S53 via the intramolecular 1,2 H-shift ( $\Delta E_a = 40.0$  kcal/mol); (3)  
664 P<sub>S26-add3</sub> converts into an alkene S54 via the elimination of hydrogen atom ( $\Delta E_a = 39.1$   
665 kcal/mol). Based on the value of  $\Delta E_a$  and the corresponding rate coefficient, the  
666 dominant pathway of the unimolecular decomposition of P<sub>S26-add3</sub> is the formation of  
667 S52.  $k_{R52}$  is about seven orders of magnitude lower than the pseudo-first-order rate  
668 constant  $k'_{R+O_2}$ , indicating that the unimolecular decomposition of P<sub>S26-add3</sub> is less  
669 importance.

670 In the presence of O<sub>2</sub>, P<sub>S26-add3</sub> can react with an O<sub>2</sub> molecule leading to the  
671 formation of the fourth generation peroxy radicals S55-x, comprising seven possible  
672 conformers as shown in Figure 7. For the intramolecular H-shifts of S55-x, not all of  
673 reactants (S55-c, S55-d and S55-e) have the suitable conformers that allow for the  
674 pathways across the reaction barriers. The barriers of intramolecular H-shifts are  
675 considerably high ( $\Delta E_a = 20.8$  kcal/mol), making them uncompetitive in the

676 atmosphere. Alternatively, S55-x can react with other RO<sub>2</sub> radicals forming an alkoxy  
677 radical S56, followed by decomposition into an alkyl radical S57 via the breakage of  
678 C<sub>4</sub>-C<sub>5</sub> bond ( $\Delta E_a = 2.0$  kcal/mol), or fragmentation into an alkyl radical S61 through  
679 the cleavage of C<sub>3</sub>-C<sub>4</sub> bond ( $\Delta E_a = 4.5$  kcal/mol). The aforementioned results reveal  
680 that the formation of S57 is energetically favorable, which is consistent with the  
681 conclusion derived from the unimolecular decomposition of S45 that the breakage of  
682 C<sub>4</sub>-C<sub>5</sub> bond is feasible. Next, S57 dissociates to a NO<sub>2</sub> coproduct and a C<sub>8</sub>-product  
683 S58 that possessed a -NO<sub>3</sub>, a peroxide bridge, two carbonyls, and three hydroxy  
684 groups. This pathway is expected to be the dominant one ( $\Delta E_a = 1.5$  kcal/mol), with  
685 the rate coefficient  $k_{RS58}$  of  $1.2 \times 10^9$  s<sup>-1</sup>. The resulting NO<sub>2</sub> can further participate in  
686 the cycling of NO<sub>x</sub>, ultimately generating tropospheric ozone and SOA.

687 The overall reaction mechanism and the fractional yields of the major products in  
688 the multi-generation OH oxidation of styrene under different NO<sub>x</sub> conditions are  
689 presented in Figures S22 and S23. In the low-NO<sub>x</sub> conditions, the fractional yield of  
690 the first generation closed-shell product 1<sup>st</sup>-ROOH (S4) formed from the reaction  
691 S2-1-x + HO<sub>2</sub>· is predicted to be 71.6%. For the second generation OH oxidation, the  
692 reaction of the peroxy radical P<sub>S4-add3-a-2</sub> with HO<sub>2</sub> radicals produces the second  
693 generation closed-shell product 2<sup>nd</sup>-ROOH (S6) and an alkoxy radical P<sub>S4-add3-a-3</sub>,  
694 with the fractional yields of 41.4% and 10.4%, respectively. The formed P<sub>S4-add3-a-2</sub>  
695 can either proceed through the C<sub>5</sub>-C<sub>6</sub> bond scission to produce an alkyl radical S7 with  
696 the fractional yield of 7.8%, or undergo via a cyclization process to generate an alkyl  
697 radical S15 with the fractional yield of 2.6%. S7 and S15 can be transformed via a  
698 series of reactions, ultimately leading to the formation of second generation  
699 closed-shell product S10-2, S13 and S23, with the fractional yields of 5.6%, 2.2% and  
700 1.3%, respectively. For the third generation OH oxidation, the degradation of  
701 2<sup>nd</sup>-ROOH (S6) ultimately yields the third generation closed-shell products S47 and  
702 S51, with the fractional yields of 26.3% and 0.3%, respectively. As a result, the major  
703 closed-shell products are 1<sup>st</sup>-ROOH (S4), 2<sup>nd</sup>-ROOH (S6), S10-2, S13 and S47 in the  
704 multi-generation OH oxidation of styrene in the low-NO<sub>x</sub> conditions.

705 In the high-NO<sub>x</sub> conditions, the fractional yield of the first generation  
706 closed-shell product 1<sup>st</sup>-RONO<sub>2</sub> (S5) formed from the reaction S2-1-x + NO is  
707 predicted to be 26.5%, as shown in Figure S23. As the OH oxidation reactions  
708 proceed, 1<sup>st</sup>-RONO<sub>2</sub> (S5) can be initially transformed into the peroxy radical  
709 P<sub>S5-add3-a-2</sub>, followed by reaction with NO to form the second generation closed-shell  
710 product 2<sup>nd</sup>-RONO<sub>2</sub> (S26) and an alkoxy radical P<sub>S5-add3-a-3</sub>, with the fractional  
711 yields of 4.8% and 11.2%, respectively. The decomposition of P<sub>S5-add3-a-3</sub> undergoes  
712 via two distinct pathways. One is the C<sub>5</sub>-C<sub>6</sub> bond cleavage, leading to an alkyl radical  
713 S27 with the fractional yield of 7.8%. The other is the cyclization, resulting in an  
714 alkyl radical S35 with the fractional yield of 3.4%. The resulting S27 and S35  
715 undergo multiple oxidation steps, finally leading to the formation of the second  
716 generation closed-shell products S30-2, S33 and S40-1, with the fractional yields of  
717 6.0%, 1.8%, and 1.7%, respectively. 2<sup>nd</sup>-RONO<sub>2</sub> (S26) can be further oxidized to  
718 yield the third generation closed-shell products S58 and S62, with the fractional yields  
719 of 2.6% and 0.03%, respectively. In summary, the major closed-shell products are  
720 1<sup>st</sup>-RONO<sub>2</sub> (S5), 2<sup>nd</sup>-RONO<sub>2</sub> (S26), S30-2 and S58 in the multi-generation OH  
721 oxidation of styrene in the high-NO<sub>x</sub> conditions.



722

723 **Figure 7.** PES for the subsequent reactions of  $\text{P}_{\text{S26-add3}}$  in the presence of  $\text{O}_2$  at the  
 724 M06-2X/6-311++G(3df,3pd)//M06-2X/6-31+g(d,p) level

### 725 3.4 Volatility Classes

726 The volatility classes for various organic compounds are based on their  
 727 saturation concentration, as proposed by Donahue et al. (2012). The saturated vapour  
 728 pressure ( $P^0$ ) and saturated concentration ( $c^0$ ) of styrene and its multi-generation OH  
 729 oxidation products are predicted by using the SIMPOL.1 method (Pankow and Asher,  
 730 2008). As show in Table S8, the  $P^0$  and  $c^0$  of the first generation closed-shell product  
 731 benzaldehyde ( $\text{C}_7\text{H}_6\text{O}$ ) are  $7.62 \times 10^{-4}$  atm and  $2.89 \times 10^6$  ug/m<sup>3</sup>, respectively, which  
 732 are 3-4 orders of magnitude greater than those of S4 ( $\text{C}_8\text{H}_{10}\text{O}_3$ ,  $P^0 = 1.43 \times 10^{-7}$  atm  
 733 and  $c^0 = 8.89 \times 10^2$  ug/m<sup>3</sup>) and S5 ( $\text{C}_8\text{H}_9\text{NO}_3$ ,  $P^0 = 2.54 \times 10^{-7}$  atm and  $c^0 = 1.87 \times$   
 734  $10^3$  ug/m<sup>3</sup>). Based on the values of  $c^0$ , benzaldehyde is classified as the volatile  
 735 organic compounds (VOCs), whereas S4 and S5 are classified as the intermediate  
 736 volatility organic compounds (IVOCs). These first generation closed-shell products  
 737 exist exclusively in the gas phase under atmospheric conditions (Bianchi et al., 2019).

738 For the second generation closed-shell products, S6 ( $C_8H_{12}O_8$ ,  $c^0 = 4.50 \times 10^{-2}$   
739  $ug/m^3$ ) and S26 ( $C_8H_{10}N_2O_{10}$ ,  $c^0 = 0.18 ug/m^3$ ) formed from the bimolecular reactions  
740 with  $HO_2$  radicals and NO are classified as the low volatility organic compounds  
741 (LVOCs). Similarly, S13 ( $C_8H_{10}O_8$ ,  $c^0 = 2.97 \times 10^{-2} ug/m^3$ ) and S33 ( $C_8H_{10}O_8$ ,  $c^0 =$   
742  $2.97 \times 10^{-2} ug/m^3$ ), formed through the ring-opening and subsequent intramolecular  
743 H-shift reactions of  $P_{S4-add3-a-3}$  and  $P_{S5-add3-a-3}$ , respectively, are also classified as  
744 LVOCs, which can condense onto the existing large particles (Bianchi et al., 2019).  
745 The  $c^0$  values of the remaining closed-shell products are significantly greater than  
746 those of the aforementioned four products, for example, the  $c^0$  values of S20 ( $C_6H_8O_6$ )  
747 and S40-1 ( $C_6H_7NO_7$ ), formed by the cyclization and decomposition reactions of  
748  $P_{S4-add3-a-3}$  and  $P_{S5-add3-a-3}$ , are 42.21 and 75.86  $ug/m^3$ , respectively, classifying them  
749 as the semivolatile organic compounds (SVOC).

750 For the third generation closed-shell products, the  $c^0$  values of S47 ( $C_8H_{12}O_9$ ,  $c^0$   
751  $= 2.68 \times 10^{-4} ug/m^3$ ) and S51 ( $C_8H_{10}O_{10}$ ,  $c^0 = 1.58 \times 10^{-4} ug/m^3$ ), formed through the  
752  $O_2$ -addition and subsequent decomposition reactions of  $P_{S6-add3}$ , are about two orders  
753 of magnitude lower than those of the second generation closed-shell products S6 and  
754 S13, despite being classified as LVOCs. Similarly, S58 ( $C_8H_{11}NO_{10}$ ,  $c^0 = 5.37 \times 10^{-4}$   
755  $ug/m^3$ ) and S62 ( $C_8H_{10}N_2O_{12}$ ,  $c^0 = 6.18 \times 10^{-4} ug/m^3$ ), formed via the  $O_2$ -addition and  
756 subsequent decomposition reactions of  $P_{S26-add3}$ , exhibit lower  $c^0$  values compared to  
757 the second generation closed-shell products S26 and S33. The aforementioned results  
758 reveal that the volatility of the multi-generation OH oxidation products significantly  
759 decreases with increasing the number of OH oxidation steps. As the oxidation  
760 reactions of the third generation closed-shell products proceed further, the formed  
761 products may possess sufficiently low volatility to participate in the formation and  
762 growth of new aerosol particle.

## 763 **4 Conclusions**

764 The formation mechanisms of highly oxidized products from the  
765 multi-generation OH oxidation of styrene under different  $NO_x$  conditions are

766 investigated by mean of quantum chemical methods. The primary conclusions are  
767 summarized as follows.

768 (a) For the first generation OH oxidation of styrene, the addition of OH radicals  
769 to terminal carbon ( $C_{\beta}$ -site) of a vinyl group is the dominant pathway. The  
770 isomerization of the first generation  $RO_2$  radicals, formed through the association  
771 reaction of OH-adduct with  $O_2$ , includes multiple intramolecular H-shift pathways  
772 with the rate coefficient  $k_{MC-TST}$  of  $1.6 \times 10^{-4} s^{-1}$ . Among the competing H-shift  
773 pathways, the hydrogen atom transfer from the  $-OH$  group to the terminal oxygen  
774 atom of the  $-OO$  group has the lowest barrier. The resulting alkoxy radical  
775 decomposes into benzaldehyde through the successive elimination of HCHO and an  
776 OH radical. Alternatively, the first generation  $RO_2$  radicals can proceed bimolecular  
777 reactions with  $HO_2$  radicals and NO, leading to the formation of the first generation  
778 closed-shell products 1<sup>st</sup>-ROOH ( $C_8H_{10}O_3$ ), benzaldehyde ( $C_7H_6O$ ), and 1<sup>st</sup>-RONO<sub>2</sub>  
779 ( $C_8H_9NO_3$ ).

780 (b) For the second generation OH oxidation of 1<sup>st</sup>-ROOH, the addition of OH  
781 radicals to  $C_1$ -site, occurring at the opposite direction relative to the  $-OOH$  group, has  
782 the smallest barrier. BPR formed by two  $O_2$ -addition steps and a cyclization process  
783 can either react with  $RO_2$  radicals to produce BAR, or interact with  $HO_2$  radicals to  
784 form the second generation closed-shell product 2<sup>nd</sup>-ROOH ( $C_8H_{12}O_8$ ). The resulting  
785 BAR may undergo via the ring-opening and subsequent decomposition reactions to  
786 generate an unsaturated 1,4-dicarbonyl compound S14 ( $C_4H_4O_2$ ), a 1,2-dicarbonyl  
787 species S10-2 ( $C_4H_6O_5$ ) and a multifunctional compound S13 ( $C_8H_{10}O_8$ ).  
788 Alternatively, it can proceed through the cyclization and subsequent dissociation  
789 reactions to produce a glycolaldehyde and a epoxide S23 ( $C_6H_6O_5$ ) containing a  
790 hydroxy and three carbonyl groups. The branching ratios of these two pathways are  
791 74.7% and 25.3%, respectively.

792 (c) For the second generation OH oxidation of 1<sup>st</sup>-RONO<sub>2</sub>, the OH-addition  
793 reaction at the  $C1$ -site, occurring at the opposite direction as the  $-ONO_2$  group, has  
794 the smallest barrier. BPR can react with NO to form BAR and the second generation  
795 closed-shell product 2<sup>nd</sup>-RONO<sub>2</sub> ( $C_8H_{10}N_2O_{10}$ ). The resulting BAR can proceed either

796 the ring opening or cyclization process to yield alkyl radicals S27 and S35, with the  
797 branching ratio of 69.2% and 30.8%. The main products of the decomposition of S27  
798 are an unsaturated 1,4-dicarbonyl compound S34 ( $C_4H_4O_2$ ), a multifunctional organic  
799 nitrate S30-2 ( $C_4H_5NO_6$ ) and a multifunctional compound S33 ( $C_8H_{10}O_8$ ). The  
800 primary products of the dissociation of S35 are a glyoxal and a  $C_6$ -epoxide specie  
801 S40-1 ( $C_6H_7NO_7$ ) containing a  $-NO_3$ , a hydroxy and two carbonyl groups.

802 (d) For the third generation OH oxidation of 2<sup>nd</sup>-ROOH and 2<sup>nd</sup>-RONO<sub>2</sub>,  
803 *syn*-OH-addition reactions occurring at the  $C_3$ -site are predominant. The alkoxy  
804 radical formed in the reaction 2<sup>nd</sup>-ROOH + OH decomposes into an OH radical  
805 byproduct and a  $C_8$ -product ( $C_8H_{12}O_9$ ) bearing a  $-OOH$ , a peroxide bridge, two  
806 carbonyls, and three hydroxy groups. The alkoxy radical formed in the reaction  
807 2<sup>nd</sup>-RONO<sub>2</sub> + OH dissociates to a NO<sub>2</sub> co-product and a  $C_8$ -product ( $C_8H_{11}NO_{10}$ )  
808 containing a  $-NO_3$ , a peroxide bridge, two carbonyls, and three hydroxy groups.

809 (e) In the low-NO<sub>x</sub> conditions, the major closed-shell products formed from the  
810 multi-generation OH oxidation of styrene are 1<sup>st</sup>-ROOH (S4), 2<sup>nd</sup>-ROOH (S6), S10-2,  
811 S13 and S47, with the fractional yields of 71.6%, 41.4%, 5.6%, 2.2% and 26.3%,  
812 respectively. In the high-NO<sub>x</sub> conditions, the major closed-shell products are  
813 1<sup>st</sup>-RONO<sub>2</sub> (S5), 2<sup>nd</sup>-RONO<sub>2</sub> (S26), S30-2 and S58, with the fractional yields of  
814 26.5%, 4.8%, 6.0% and 2.6%, respectively.

815 (f) The first generation closed-shell products 1<sup>st</sup>-ROOH ( $C_8H_{10}O_3$ ) and  
816 1<sup>st</sup>-RONO<sub>2</sub> ( $C_8H_9NO_3$ ) are classified as IVOCs, which exist exclusively in the gas  
817 phase in the atmosphere. The second generation closed-shell products, S6 ( $C_8H_{12}O_8$ ),  
818 S26 ( $C_8H_{10}N_2O_{10}$ ), S13 ( $C_8H_{10}O_8$ ) and S33 ( $C_8H_{10}O_8$ ) are classified as LVOCs, which  
819 can condense onto the existing large particles. The third generation closed-shell  
820 products S47 ( $C_8H_{12}O_9$ ), S51 ( $C_8H_{10}O_{10}$ ), S58 ( $C_8H_{11}NO_{10}$ ) and S62 ( $C_8H_{10}N_2O_{10}$ )  
821 exhibit lower  $c^0$  values compared to the second generation closed-shell products,  
822 despite being classified as LVOCs. As a result, the volatility of the  
823 multi-generation OH oxidation products significantly decreases with increasing the  
824 number of OH oxidation steps.

825

## 826 **Data availability**

827 The data are accessible by contacting the corresponding author  
828 (huangyu@ieecas.cn).

829

## 830 **Supplement**

831 Tables S1 and S3 list the energy barriers of all the elementary reactions involved  
832 in the addition of OH radicals to styrene and 1<sup>st</sup>-ROOH (S4) predicted at different  
833 levels. Tables S2, S4 and S6 list the relative electronic energy, free energy and  
834 Boltzmann population of different conformers involved in S2-1-x, S8-x and S28-x.  
835 Tables S5 and S7 list the MC-TST rate coefficients for the intramolecular H-shift  
836 reactions of S8-x and S28-x. Table S8 summaries the saturated vapour pressure and  
837 saturated concentrations of styrene and its multiple generation OH oxidation  
838 closed-shell products. Figures S1-S3 display the PESs for the unimolecular reactions  
839 of S2-2-x, S2-3-x and S2-4-x. Figure S4 shows the global minimum structures of  
840 1<sup>st</sup>-ROOH(S4) and 1<sup>st</sup>-RONO<sub>2</sub>(S5). Figure S5 depicts the geometric parameters of  
841 toluene and 1<sup>st</sup>-ROOH (S4) and the NPA atomic charges of all the carbon atoms.  
842 Figures S6 and S11 show the PESs for the addition reactions P<sub>S4-add1</sub> + O<sub>2</sub> and P<sub>S5-add1</sub>  
843 + O<sub>2</sub>. Figures S7 and S12 present the lowest energy conformers of third generation  
844 peroxy radicals P<sub>S4-add3-a-2</sub> and P<sub>S5-add3-a-2</sub>. Figures S8-S10 depict the PESs for the  
845 intramolecular hydrogen transfer reactions of S8-x, S12-x and S16-x. Figures  
846 S13-S15 depict the PESs for the intramolecular hydrogen transfer reactions of S28-x,  
847 S32-x and S36-x. Figures S16-18 show the PESs for the OH-initiated oxidation of  
848 2<sup>nd</sup>-ROOH (S6) and unimolecular decomposition of P<sub>S6-add3</sub>. Figures S19-S21 show  
849 the PESs for the OH-initiated oxidation of 2<sup>nd</sup>-RONO<sub>2</sub> (S26) and unimolecular  
850 decomposition of P<sub>S26-add3</sub>. Figures S22 and S23 show the overall reaction mechanism  
851 of the multi-generation OH oxidation of styrene in the low- and high-NO<sub>x</sub> conditions.

852

## 853 **Author contribution**

854 LC and YH conceptualized the study. LC conducted quantum chemical

855 calculation. YX and ZJ analyzed the data. LC conducted the volatility estimation. All  
856 authors discussed the results and commented on the manuscript.

857

## 858 **Competing interests**

859 The contact author has declared that none of the authors has any competing interests.

860

## 861 **Financial support**

862 This study was supported by the National Natural Science Foundation of China (grant  
863 nos. 42175134) and the Youth Innovation Promotion Association of the Chinese  
864 Academy of Sciences (grant number 2022415).

865

## 866 **Reference**

- 867 Alecu, I. M., Zheng, J., Zhao, Y., and Truhlar, D. G.: Computational thermochemistry: scale factor  
868 databases and scale factors for vibrational frequencies obtained from electronic model  
869 chemistries, *J. Chem. Theory Comput.*, 6, 2872-2887, <https://doi.org/10.1021/ct100326h>,  
870 2010.
- 871 Arathala, P., and Musah, R. A.: Atmospheric chemistry of chloroprene initiated by OH radicals:  
872 combined Ab initio/DFT calculations and kinetics analysis, *J. Phys. Chem. A*, 128,  
873 8983-8995, <https://doi.org/10.1021/acs.jpca.4c05428>, 2024.
- 874 Atkinson, R., and Arey, J.: Atmospheric degradation of volatile organic compounds, *Chem. Rev.*,  
875 103, 4605-4638, <https://doi.org/10.1021/cr0206420>, 2003.
- 876 Bianchi, F., Kurten, T., Riva, M., Mohr, C., Rissanen, M. P., Roldin, P., Berndt, T., Crouse, J. D.,  
877 Wennberg, P. O., Mentel, T. F., Wildt, J., Junninen, H., Jokinen, T., Kulmala, M., Worsnop, D.  
878 R., Thornton, J. A., Donahue, N., Kjaergaard, H. G., and Ehn, M.: Highly oxygenated organic  
879 molecules (HOM) from gas-phase autoxidation involving peroxy radicals: a key contributor  
880 to atmospheric aerosol, *Chem. Rev.*, 119, 3472-3509,  
881 <https://doi.org/10.1021/acs.chemrev.8b00395>, 2019.
- 882 Bloss, C., Wagner, V., Jenkin, M. E., Volkamer, R., Bloss, W. J., Lee, J. D., Heard, D. E., Wirtz, K.,  
883 Martin-Reviejo, M., Rea, G., Wenger, J. C., and Pilling, M. J.: Development of a detailed  
884 chemical mechanism (MCMv3.1) for the atmospheric oxidation of aromatic hydrocarbons,  
885 *Atmos. Chem. Phys.*, 5, 641-664, <https://doi.org/10.5194/acp-5-641-2005>, 2005.
- 886 Boyd, A. A., Flaud, P. M., Daugey, N., and Lesclaux, R.: Rate constants for RO<sub>2</sub> + HO<sub>2</sub> reactions  
887 measured under a large excess of HO<sub>2</sub>, *J. Phys. Chem. A*, 107, 818-821,  
888 <https://doi.org/10.1021/jp026581r>, 2003.
- 889 Cabrera-Perez, D., Taraborrelli, D., Sander, R., and Pozzer, A.: Global atmospheric budget of  
890 simple monocyclic aromatic compounds, *Atmos. Chem. Phys.*, 16, 6931-6947,  
891 <https://doi.org/10.5194/acp-16-6931-2016>, 2016.

892 Canneaux, S., Bohr, F., and Henon, E.: KiSTheIP: a program to predict thermodynamic properties  
893 and rate constants from quantum chemistry results, *J. Comput. Chem.*, 35, 82-93,  
894 <https://doi.org/10.1002/jcc.23470>, 2013.

895 Chen, L., Huang, Y., Xue, Y., Jia, Z., and Wang, W.: Atmospheric oxidation of 1-butene initiated  
896 by OH radical: Implications for ozone and nitrous acid formations, *Atmos. Environ.*, 244,  
897 118010-118021, <https://doi.org/10.1016/j.atmosenv.2020.118010>, 2021.

898 Cho, J., Roueintan, M., and Li, Z.: Kinetic and dynamic investigations of OH reaction with  
899 styrene, *J. Phys. Chem. A*, 118, 9460-9470, <https://doi.org/10.1021/jp501380j>, 2014.

900 Donahue, N. M., Kroll, J. H., Pandis, S. N., and Robinson, A. L.: A two-dimensional volatility  
901 basis set – Part 2: Diagnostics of organic-aerosol evolution, *Atmos. Chem. Phys.*, 12,  
902 615-634, <https://doi.org/10.5194/acp-12-615-2012>, 2012.

903 Eckart, C.: The penetration of a potential barrier by electrons, *Phys. Rev.*, 35, 1303-1309,  
904 <https://doi.org/10.1103/PhysRev.35.1303>, 1930.

905 Environmental Protection Agency (EPA). Clean Air Act: Title I-Air Pollution Prevention and  
906 Control. U.S. 1990.

907 Fernández-Ramos, A., Ellingson, B. A., Meana-Pañeda, R., Marques, J. M. C., and Truhlar, D. G.:  
908 Symmetry numbers and chemical reaction rates, *Theor. Chem. Acc.*, 118, 813-826,  
909 <https://doi.org/10.1007/s00214-007-0328-0>, 2007.

910 Forstner, H. J. L., Flagan, R. C., and Seinfeld, J. H.: Secondary organic aerosol from the  
911 photooxidation of aromatic hydrocarbons: molecular composition, *Environ. Sci. Technol.*, 31,  
912 1345-1358, <https://doi.org/10.1021/es9605376>, 1997.

913 Frisch, M. J., Trucks, G. W., Schlegel, H. B., Scuseria, G. E., Robb, M. A., Cheeseman, J. R.,  
914 Scalmani, G., Barone, V., Petersson, G. A., Nakatsuji, H., Li, X., Caricato, M., Marenich, A.  
915 V., Bloino, J., Janesko, B. G., Gomperts, R., Mennucci, B., Hratchian, H. P., Ortiz, J. V.,  
916 Izmaylov, A. F., Sonnenberg, J. L., Williams-Young, D., Ding, F., Lipparini, F., Egidi, F.,  
917 Goings, J., Peng, B., Petrone, A., Henderson, T., Ranasinghe, D., Zakrzewski, V. G., Gao, J.,  
918 Rega, N., Zheng, G., Liang, W., Hada, M., Ehara, M., Toyota, K., Fukuda, R., Hasegawa, J.,  
919 Ishida, M., Nakajima, T., Honda, Y., Kitao, O., Nakai, H., Vreven, T., Throssell, K.,  
920 Montgomery, J. A., Peralta, J. J. E., Ogliaro, F., Bearpark, M. J., Heyd, J. J., Brothers, E. N.,  
921 Kudin, K. N., Staroverov, V. N., Keith, T. A., Kobayashi, R., Normand, J., Raghavachari, K.,  
922 Rendell, A. P., Burant, J. C., Iyengar, S. S., Tomasi, J., Cossi, M., Millam, J. M., Klene, M.,  
923 Adamo, C., Cammi, R., Ochterski, J. W., Martin, R. L., Morokuma, K., Farkas, O., Foresman,  
924 J. B., and Fox, D. J.: Gaussian 16, Revision B.01, Gaussian, Inc., Wallingford CT, 2016.

925 Fu, Z., Guo, S., Xie, H. B., Zhou, P., Boy, M., Yao, M., and Hu, M.: A near-explicit reaction  
926 mechanism of chlorine-initiated limonene: implications for health risks associated with the  
927 concurrent use of cleaning agents and disinfectants, *Environ. Sci. Technol.*, 58, 19762-19773,  
928 <https://doi.org/10.1021/acs.est.4c04388>, 2024.

929 Fu, Z., Ma, F., Liu, Y., Yan, C., Huang, D., Chen, J., Elm, J., Li, Y., Ding, A., Pichelstorfer, L., Xie,  
930 H. B., Nie, W., Francisco, J. S., and Zhou, P.: An overlooked oxidation mechanism of toluene:  
931 computational predictions and experimental validations, *Chem. Sci.*, 14, 13050-13059,  
932 <https://doi.org/10.1039/D3SC03638C>, 2023.

933 Fu, Z., Xie, H. B., Elm, J., Guo, X., Fu, Z., and Chen, J.: Formation of low-volatile products and  
934 unexpected high formaldehyde yield from the atmospheric oxidation of methylsiloxanes,  
935 *Environ. Sci. Technol.*, 54, 7136-7145, <https://doi.org/10.1021/acs.est.0c01090>, 2020.

936 Fukui, K.: The path of chemical reactions - the IRC approach, *Acc. Chem. Res.*, 14, 363-368,  
937 <https://doi.org/10.1021/ar00072a001>, 1981.

938 Garmash, O., Rissanen, M. P., Pullinen, I., Schmitt, S., Kausiala, O., Tillmann, R., Zhao, D.,  
939 Percival, C., Bannan, T. J., Priestley, M., Hallquist, Å M., Kleist, E., Kiendler-Scharr, A.,  
940 Hallquist, M., Berndt, T., McFiggans, G., Wildt, J., Mentel, T. F., and Ehn, M.:  
941 Multi-generation OH oxidation as a source for highly oxygenated organic molecules from  
942 aromatics, *Atmos. Chem. Phys.*, 20, 515-537, <https://doi.org/10.5194/acp-20-515-2020>, 2020.

943 Gilbert, R. G., and Smith, S. C.: *Theory of unimolecular and recombination reactions*, Blackwell  
944 Scientific: Carlton, Australia, 1990.

945 Glowacki, D. R., Liang, C. H., Morley, C., Pilling, M. J., and Robertson, S. H.: MESMER: an  
946 open-source master equation solver for multi-energy well reactions, *J. Phys. Chem. A*, 116,  
947 9545-9560, <https://doi.org/10.1021/jp3051033>, 2012.

948 Holbrook, K. A., Pilling, M. J., Robertson, S. H., and Robinson, P. J.: *Unimolecular reactions*, 2nd  
949 ed.; Wiley: New York, 1996.

950 Huang, Y., Su, T., Wang, L., Wang, N., Xue, Y., Dai, W., Lee, S. C., Cao, J., and Ho, S. S. H.:  
951 Evaluation and characterization of volatile air toxics indoors in a heavy polluted city of  
952 northwestern China in wintertime, *Sci. Total Environ.*, 662, 470-480,  
953 <https://doi.org/10.1016/j.scitotenv.2019.01.250>, 2019.

954 Iuga, C., Galano, A., and Vivier-Bunge, A.: Theoretical investigation of the OH-initiated oxidation  
955 of benzaldehyde in the troposphere, *Chem. Phys. Chem.*, 9, 1453-1459,  
956 <https://doi.org/10.1002/cphc.200800144>, 2008.

957 Iyer, S., Kumar, A., Savolainen, A., Barua, S., Daub, C., Pichelstorfer, L., Roldin, P., Garmash, O.,  
958 Seal, P., Kurtén, T., and Rissanen, M.: Molecular rearrangement of bicyclic peroxy radicals is  
959 a key route to aerosol from aromatics, *Nat. Commun.*, 14, 4984-4991,  
960 <https://doi.org/10.1038/s41467-023-40675-2>, 2023.

961 Ji, Y., Zhao, J., Terazono, H., Misawa, K., Levitt, N. P., Li, Y., Lin, Y., Peng, J., Wang, Y., Duan, L.,  
962 Pan, B., Zhang, F., Feng, X., An, T., Marrero-Ortiz, W., Secret, J., Zhang, A. L., Shibuya, K.,  
963 Molina, M. J., and Zhang, R.: Reassessing the atmospheric oxidation mechanism of toluene,  
964 *Proc. Natl. Acad. Sci. U.S.A.*, 114, 8169-8174, <https://doi.org/10.1073/pnas.1705463114>,  
965 2017.

966 Koppmann, R.: *Volatile organic compounds in the atmosphere*, John Wiley & Sons, 2008.

967 Li, M., Zhang, Q., Zheng, B., Tong, D., Lei, Y., Liu, F., Hong, C., Kang, S., Yan, L., Zhang, Y., Bo,  
968 Y., Su, H., Cheng, Y., and He, K.: Persistent growth of anthropogenic non-methane volatile  
969 organic compound (NMVOC) emissions in China during 1990-2017: drivers, speciation and  
970 ozone formation potential, *Atmos. Chem. Phys.*, 19, 8897-8913,  
971 <https://doi.org/10.5194/acp-19-8897-2019>, 2019.

972 Lu, T.: Molclus program, Version 1.9.3. <http://www.keinsci.com/research/molclus.html> (accessed  
973 May 21, 2024).

974 Ma, F., Guo, X., Xia, D., Xie, H. B., Wang, Y., Elm, J., Chen, J., and Niu, J.: Atmospheric  
975 chemistry of allylic radicals from isoprene: a successive cyclization-driven autoxidation  
976 mechanism, *Environ. Sci. Technol.*, 55, 4399-4409, <https://doi.org/10.1021/acs.est.0c07925>,  
977 2021.

978 Møller, K. H., Berndt, T., and Kjaergaard, H. G.: Atmospheric autoxidation of amines, *Environ.*  
979 *Sci. Technol.*, 54, 11087-11099, <https://doi.org/10.1021/acs.est.0c03937>, 2020.

980 Møller, K. H., Otkjær, R. V., Hyttinen, N., Kurtén, T., and Kjaergaard, H. G.: Cost-effective  
981 implementation of multiconformer transition state theory for peroxy radical hydrogen shift  
982 reactions, *J. Phys. Chem. A*, 120, 10072-10087, <https://doi.org/10.1021/acs.jpca.6b09370>,  
983 2016.

984 Molteni, U., Bianchi, F., Klein, F., Haddad, I. E., Frege, C., Rossi, M. J., Dommen, J., and  
985 Baltensperger, U.: Formation of highly oxygenated organic molecules from aromatic  
986 compounds, *Atmos. Chem. Phys.*, 18, 1909-1921, <https://doi.org/10.5194/acp-18-1909-2018>,  
987 2018.

988 Neese, F.: Software update: the ORCA program system—version 6.0, *Wires Comput. Mol. Sci.*, 15,  
989 e70019, <https://doi.org/10.1002/wcms.70019>, 2025.

990 Nie, W., Yan, C., Huang, D. D., Wang, Z., Liu, Y., Qiao, X., Guo, Y., Tian, L., Zheng, P., Xu, Z., Li,  
991 Y., Xu, Z., Qi, X., Sun, P., Wang, J., Zheng, F., Li, X., Yin, R., Dallenbach, K. R., Bianchi, F.,  
992 Petäjä T., Zhang, Y., Wang, M., Schervish, M., Wang, S., Qiao, L., Wang, Q., Zhou, M.,  
993 Wang, H., Yu, C., Yao, D., Guo, H., Ye, P., Lee, S., Li, Y. J., Liu, Y., Chi, X., Kerminen, V. M.,  
994 Ehn, M., Donahue, N. M., Wang, T., Huang, C., Kulmala, M., Worsnop, D., Jiang, J., and  
995 Ding, A.: Secondary organic aerosol formed by condensing anthropogenic vapours over  
996 China's megacities, *Nat. Geosci.*, 15, 255-261, <https://doi.org/10.1038/s41561-022-00922-5>,  
997 2022.

998 Orlando, J. J., and Tyndall, G. S.: Laboratory studies of organic peroxy radical chemistry: an  
999 overview with emphasis on recent issues of atmospheric significance, *Chem. Soc. Rev.*, 41,  
1000 6294-6317, <https://doi.org/10.1039/C2CS35166H>, 2012.

1001 Pankow, J. F., and Asher, W. E.: SIMPOL.1: a simple group contribution method for predicting  
1002 vapor pressures and enthalpies of vaporization of multifunctional organic compounds, *Atmos.*  
1003 *Chem. Phys.*, 8, 2773-2796, <https://doi.org/10.5194/acp-8-2773-2008>, 2008.

1004 Pasik, D., Frandsen, B. N., Meder, M., Iyer, S., Kurtén, T., and Myllys, N.: Gas-phase oxidation of  
1005 atmospherically relevant unsaturated hydrocarbons by acyl peroxy radicals, *J. Am. Chem.*  
1006 *Soc.*, 146, 13427-13437, <https://doi.org/10.1021/jacs.4c02523>, 2024.

1007 Sebbar, N., Bozzelli, J. W., and Bockhorn, H.: Thermochemistry and reaction paths in the  
1008 oxidation reaction of benzoyl radical: C<sub>6</sub>H<sub>5</sub>C(=O), *J. Phys. Chem. A*, 115, 11897-11914,  
1009 <https://doi.org/10.1021/jp2078067>, 2011.

1010 Shen, H., Vereecken, L., Kang, S., Pullinen, I., Fuchs, H., Zhao, D., and Mentel, T. F.: Unexpected  
1011 significance of a minor reaction pathway in daytime formation of biogenic highly oxygenated  
1012 organic compounds, *Sci. Adv.*, 8, eabp8702, <https://doi.org/10.1126/sciadv.abp8702>, 2022.

1013 Sun, J., Wu, F., Hu, B., Tang, G., Zhang, J., and Wang, Y.: VOC characteristics, emissions and  
1014 contributions to SOA formation during hazy episodes, *Atmos. Environ.*, 141, 560-570,  
1015 <https://doi.org/10.1016/j.atmosenv.2016.06.060>, 2016.

1016 Tajuelo, M., Bravo, I., Rodríguez, A., Aranda, A., D'Áz-de-Mera, Y., and Rodríguez, D.:  
1017 Atmospheric sink of styrene,  $\alpha$ -methylstyrene, trans- $\beta$ -methylstyrene and indene: Rate  
1018 constants and mechanisms of Cl atom-initiated degradation, *Atmos. Environ.*, 200, 78-89,  
1019 <https://doi.org/10.1016/j.atmosenv.2018.11.059>, 2019c.

1020 Tajuelo, M., Rodríguez, A., Baeza-Romero, M. T., Aranda, A., D'Áz-de-Mera, Y., and Rodríguez,  
1021 D.: Secondary organic aerosol formation from  $\alpha$ -methylstyrene atmospheric degradation:  
1022 Role of NO<sub>x</sub> level, relative humidity and inorganic seed aerosol, *Atmos. Res.*, 230,  
1023 104631-104640, <https://doi.org/10.1016/j.atmosres.2019.104631>, 2019b.

1024 Tajuelo, M., Rodríguez, D., Baeza-Romero, M. T., Díez-de-Mera, Y., Aranda, A., and Rodríguez,  
1025 A.: Secondary organic aerosol formation from styrene photolysis and photooxidation with  
1026 hydroxyl radicals, *Chemosphere*, 231, 276-286,  
1027 <https://doi.org/10.1016/j.chemosphere.2019.05.136>, 2019a.

1028 Vereecken, L., Glowacki, D. R., and Pilling, M. J.: Theoretical chemical kinetics in tropospheric  
1029 chemistry: methodologies and applications, *Chem. Rev.*, 115, 4063-4114,  
1030 <https://doi.org/10.1021/cr500488p>, 2015.

1031 Wang, H., Ji, Y., Gao, Y., Li, G., and An, T.: Theoretical model on the formation possibility of  
1032 secondary organic aerosol from OH initiated oxidation reaction of styrene in the presence of  
1033 O<sub>2</sub>/NO, *Atmos. Environ.*, 101, 1-9, <https://doi.org/10.1016/j.atmosenv.2014.10.042>, 2015.

1034 Wang, L., Wu, R., and Xu, C.: Atmospheric oxidation mechanism of benzene. Fates of alkoxy  
1035 radical intermediates and revised mechanism, *J. Phys. Chem. A*, 117, 14163-14168,  
1036 <https://doi.org/10.1021/jp4101762>, 2013.

1037 Wang, M., Chen, D., Xiao, M., Ye, Q., Stolzenburg, D., Hofbauer, V., Ye, P., Vogel, A. L., Mauldin,  
1038 R. L., Amorim, A., Baccharini, A., Baumgartner, B., Brilke, S., Dada, L., Dias, A., Duplissy, J.,  
1039 Finkenzeller, H., Garmash, O., He, X. C., Hoyle, C. R., Kim, C., Kvashnin, A., Lehtipalo, K.,  
1040 Fischer, L., Molteni, U., Petřáková T., Pospisilova, V., Quéléver, L. L. J., Rissanen, M., Simon,  
1041 M., Tauber, C., Tomé A., Wagner, A. C., Weitz, L., Volkamer, R., Winkler, P. M., Kirkby, J.,  
1042 Worsnop, D. R., Kulmala, M., Baltensperger, U., Dommen, J., El-Haddad, I., and Donahue,  
1043 N. M.: Photo-oxidation of aromatic hydrocarbons produces low-volatility organic compounds,  
1044 *Environ. Sci. Technol.*, 54, 7911-7921, <https://doi.org/10.1021/acs.est.0c02100>, 2020.

1045 Wang, S., and Li, H.: NO<sub>3</sub>-initiated gas-phase formation of nitrated phenolic compounds in  
1046 polluted atmosphere, *Environ. Sci. Technol.*, 55, 2899-2907,  
1047 <https://doi.org/10.1021/acs.est.0c08041>, 2021.

1048 Wang, S., Newland, M. J., Deng, W., Rickard, A. R., Hamilton, J. F., Muñoz, A., Ródenas, M.,  
1049 Vázquez, M. M., Wang, L., and Wang, X.: Aromatic photo-oxidation, a new source of  
1050 atmospheric acidity, *Environ. Sci. Technol.*, 54, 7798-7806,  
1051 <https://doi.org/10.1021/acs.est.0c00526>, 2020.

1052 Wang, S., Wu, R., Berndt, T., Ehn, M., and Wang, L.: Formation of highly oxidized radicals and  
1053 multifunctional products from the atmospheric oxidation of alkylbenzene, *Environ. Sci.*  
1054 *Technol.*, 51, 8442-8449, <https://doi.org/10.1021/acs.est.7b02374>, 2017.

1055 Wu, R., Pan, S., Li, Y., and Wang, L.: Atmospheric oxidation mechanism of toluene, *J. Phys.*  
1056 *Chem. A*, 118, 4533-4547, <https://doi.org/10.1021/jp500077f>, 2014.

1057 Wu, X., Hou, Q., Huang, J., Chai, J., and Zhang, F.: Exploring the OH-initiated reactions of  
1058 styrene in the atmosphere and the role of van der Waals complex, *Chemosphere*, 282,  
1059 131004-131012, <https://doi.org/10.1016/j.chemosphere.2021.131004>, 2021.

1060 Wu, X., Huang, C., Niu, S., and Zhang, F.: New theoretical insights into the reaction kinetics of  
1061 toluene and hydroxyl radicals, *Phys. Chem. Chem. Phys.*, 22, 22279-22288,  
1062 <https://doi.org/10.1039/D0CP02984J>, 2020.

1063 Xu, L., Møller, K. H., Crounse, J. D., Kjaergaard, H. G., and Wennberg, P. O.: New insights into  
1064 the radical chemistry and product distribution in the OH-initiated oxidation of benzene,  
1065 *Environ. Sci. Technol.*, 54, 13467-13477, <https://doi.org/10.1021/acs.est.0c04780>, 2020.

1066 Yan, Y., Cabrera-Perez, D., Lin, J., Pozzer, A., Hu, L., Millet, D. B., Porter, W. C., and Lelieveld,  
1067 J.: Global tropospheric effects of aromatic chemistry with the SAPRC-11 mechanism

1068 implemented in GEOS-Chem version 9-02, *Geosci. Model Dev.*, 12, 111-130,  
1069 <https://doi.org/10.5194/gmd-12-111-2019>, 2019.

1070 Yang, F., Deng, F., Pan, Y., Zhang, Y., Tang, C., and Huang, Z.: Kinetics of hydrogen abstraction  
1071 and addition reactions of 3-hexene by OH radicals, *J. Phys. Chem. A*, 121, 1877-1889,  
1072 <https://doi.org/10.1021/acs.jpca.6b11499>, 2017.

1073 Yu, S., Jia, L., Xu, Y., and Pan, Y.: Formation of extremely low-volatility organic compounds from  
1074 styrene ozonolysis: Implication for nucleation, *Chemosphere*, 305, 135459-135467,  
1075 <https://doi.org/10.1016/j.chemosphere.2022.135459>, 2022.

1076 Yu, S., Jia, L., Xu, Y., and Pan, Y.: Molecular composition of secondary organic aerosol from  
1077 styrene under different NO<sub>x</sub> and humidity conditions, *Atmos. Res.*, 266, 105950-10604,  
1078 <https://doi.org/10.1016/j.atmosres.2021.105950>, 2022.

1079 Zaytsev, A., Koss, A. R., Breitenlechner, M., Krechmer, J. E., Nihill, K. J., Lim, C. Y., Rowe, J. C.,  
1080 Cox, J. L., Moss, J., Roscioli, J. R., Canagaratna, M. R., Worsnop, D. R., Kroll, J. H., and  
1081 Keutsch, F. N.: Mechanistic study of the formation of ring-retaining and ring-opening  
1082 products from the oxidation of aromatic compounds under urban atmospheric conditions,  
1083 *Atmos. Chem. Phys.*, 19, 15117-15129, <https://doi.org/10.5194/acp-19-15117-2019>, 2019.

1084 Zhang, H., Wang, J., Dong, B., Xu, F., Liu, H., Zhang, Q., Zong, W., and Shi, X.: New mechanism  
1085 for the participation of aromatic oxidation products in atmospheric nucleation, *Sci. Total*  
1086 *Environ.*, 917, 170487-170494, <https://doi.org/10.1016/j.scitotenv.2024.170487>, 2024.

1087 Zhang, R. M., Truhlar, D. G., and Xu, X.: Kinetics of the toluene reaction with OH radical,  
1088 *Research*, 2019, Article ID 5373785, <https://doi.org/10.34133/2019/5373785>, 2019.

1089 Zhao, H., Zhang, Y., Zhao, Q., Li, Y., and Huang, Z.: A theoretical study of H-abstractions of  
1090 benzaldehyde by H, O<sup>3</sup>(P), <sup>3</sup>O<sub>2</sub>, OH, HO<sub>2</sub>, and CH<sub>3</sub> radicals: Ab initio rate coefficients and  
1091 their uncertainty quantification, *J. Phys. Chem. A*, 126, 7523-7533,  
1092 <https://doi.org/10.1021/acs.jpca.2c02384>, 2022.

1093 Zhao, Y., and Truhlar, D. G.: The M06 suite of density functionals for main group  
1094 thermochemistry, thermochemical kinetics, noncovalent interactions, excited states, and  
1095 transition elements: two new functionals and systematic testing of four M06-class functionals  
1096 and 12 other functionals, *Theor. Chem. Acc.*, 120, 215-241,  
1097 <https://doi.org/10.1007/s00214-007-0310-x>, 2008.

1098